



TECHNISCHE
UNIVERSITÄT
WIEN

DIPLOMARBEIT

Dynamic 3D Relaxation Time Mapping of Deuterium (^2H) Labeled Resonances in the Human Brain at 7T

zur Erlangung des akademischen Grades

Diplom-Ingenieurin

im Rahmen des Studiums

Technische Physik

eingereicht von

Viola Bader, BSc

Matrikelnummer: 11776213

ausgeführt am **Institut für Angewandte Physik** der Technischen Universität Wien
in Zusammenarbeit mit dem **Hochfeld MR Zentrum** der Medizinischen Universität Wien

Betreuung:

Ao. Univ. Prof. Dipl.-Ing. Dr.techn. Martin Gröschl

unter lokaler Betreuung von:

Assoc. Prof. Dipl.-Ing. Dr.techn. Wolfgang Bogner,

Dipl.-Ing. Fabian Niess, PhD

02.02.2024

Unterschrift Betreuer

Unterschrift Studentin

Abstract

Impaired glucose metabolism plays an important role in many common brain diseases such as cancer, neurodegenerative diseases or diabetes. Deuterium metabolic imaging (DMI) is an emerging Magnetic Resonance technique to non-invasively map the cellular glucose uptake and downstream metabolism. For a reliable concentration estimation, tissue-specific relaxation times are essential, yet only unlocalized relaxation time constants of deuterium labeled resonances are reported.

The aim of this thesis was to measure tissue-specific longitudinal and transversal relaxation times of deuterated resonances (glucose, glutamate+glutamine) in the healthy human brain after oral administration of deuterium labeled glucose. Hence, Inversion recovery and Hahn spin-echo acquisition schemes were implemented into a 3D free induction decay Magnetic Resonance spectroscopic imaging sequence featuring a fast non-Cartesian concentric ring trajectory readout.

Following validation of the sequence in vitro using a water phantom, eight healthy volunteers were measured after oral administration of deuterated glucose. Tissue-specific T_1 and T_2 relaxation time constants of Glc ($T_1^{\text{GM}} = 56 \pm 14$ ms; $T_1^{\text{WM}} = 60 \pm 19$ ms; $T_2^{\text{GM}} = 37 \pm 1$ ms; $T_2^{\text{WM}} = 36 \pm 2$ ms) and Glx ($T_1^{\text{GM}} = 167 \pm 22$ ms; $T_1^{\text{WM}} = 173 \pm 12$ ms; $T_2^{\text{GM}} = 36 \pm 1$ ms; $T_2^{\text{WM}} = 34 \pm 1$ ms) were not significantly different between GM and WM.

One volunteer was additionally remeasured without glucose administration to determine relaxation times of the natural abundance water ($T_1^{\text{GM}} = 352 \pm 15$ ms; $T_2^{\text{GM}} = 36 \pm 1$ ms; $T_1^{\text{WM}} = 311 \pm 13$ ms; $T_2^{\text{WM}} = 31 \pm 1$ ms).

The developed sequence can be in principle applied to other nuclei e.g., ^1H or ^{31}P MRSI, potentially improving the specificity to detect small local variations in relaxation times, as often observed for certain pathologies and ultimately improve the accuracy of concentration estimation in future studies.

Zusammenfassung

Viele Erkrankungen des menschlichen Gehirns wie z.B. Krebs, neurodegenerative Pathologien oder Diabetes sind durch eine Störung des Glukosestoffwechsels gekennzeichnet. Deuterium metabolic imaging (DMI) ist eine vielversprechende Methode der Magnetresonanzbildgebung, welche nicht-invasiven Einblick in dynamische Prozesse des intrazellulären Glukosestoffwechsels ermöglicht. Für präzisere Konzentrationsabschätzungen wären gewebespezifische Relaxationszeiten von entscheidender Bedeutung. Bisher wurden jedoch ausschließlich unlokalisierte Relaxationszeiten von deuterierten Substanzen publiziert.

Ziel dieser Diplomarbeit ist die Erfassung gewebespezifischer Relaxationszeiten von deuterierten Substanzen (Glukose, Glutamat+Glutamin) im gesunden menschlichen Gehirn. Zu diesem Zweck wurden Inversion-Recovery und Hahn-Spin-Echo Akquisitionsmethoden in eine existierende 3D free induction decay Magnetresonanztomographie-bildgebungssequenz implementiert.

Die Funktionalität der entwickelten Pulssequenz wurde anhand von in vitro Messungen an einem Wasserphantom validiert. Anschließend wurde das Gehirn acht gesunder Probanden, unmittelbar nach oraler Verabreichung von deuterierter Glukose untersucht. Relaxationszeiten in grauer und weißer Substanz von Glc ($T_1^{\text{GM}} = 56 \pm 14$ ms; $T_1^{\text{WM}} = 60 \pm 19$ ms; $T_2^{\text{GM}} = 37 \pm 1$ ms; $T_2^{\text{WM}} = 36 \pm 2$ ms) und Glx ($T_1^{\text{GM}} = 167 \pm 22$ ms; $T_1^{\text{WM}} = 173 \pm 12$ ms; $T_2^{\text{GM}} = 36 \pm 1$ ms; $T_2^{\text{WM}} = 34 \pm 1$ ms) waren nicht signifikant unterschiedlich. Um gewebespezifische Relaxationszeiten von Wasser zu messen, wurde zusätzlich ein Proband

ohne Verabreichung von deuterierter Glukose gemessen ($T_1^{\text{GM}} = 352 \pm 15 \text{ ms}$; $T_2^{\text{GM}} = 36 \pm 1 \text{ ms}$; $T_1^{\text{WM}} = 311 \pm 13 \text{ ms}$; $T_2^{\text{WM}} = 31 \pm 1 \text{ ms}$).

Die entwickelte Pulssequenz kann prinzipiell auf beliebig andere Kerne angewendet werden, wie z.B. ^1H oder ^{31}P . Dies könnte die Spezifität zur Erkennung kleiner lokaler Änderungen von Relaxationszeiten verbessern, wie sie häufig bei bestimmten Pathologien beobachtet werden, und letztendlich die Genauigkeit der Konzentrationsabschätzung in zukünftigen Studien verbessern.

Acknowledgements

I would like to thank Wolfgang Bogner for giving me the opportunity to do my master's thesis in his group. A special thanks goes to Fabian Niess for the kind supervision throughout this master thesis and also project thesis. Thank you for the many helpful discussions, feedback and for always having an open ear if I needed some advice.

I want to thank the whole group for welcoming me into your team and for creating such an enjoyable working atmosphere. It has been a pleasure to work with you and I am looking forward to continue being part of your team in the future.

I would also like to thank Martin Gröschl for the supervision from the Technical University's side.

A big thank you to all my friends who made my study life more enjoyable. A shout-out goes to my 'Laborbuddy', Lea, who added a lot of fun to the many long days we spent in the lab during courses.

Last but foremost, I want to express my deepest gratitude to the most important people in my life: my parents Franz and Lucia, my sister Luca (Lux) and especially my girlfriend Laura (Bebe) for their unwavering support. Thank you all for always being there for me and cheering me up when I needed encouragement. I couldn't have accomplished this without all of you.

Eidesstaatliche Erklärung

Ich erkläre an Eides statt, dass die vorliegende Arbeit nach den anerkannten Grundsätzen für wissenschaftliche Abhandlungen von mir selbstständig erstellt wurde. Alle verwendeten Hilfsmittel, insbesondere die zugrunde gelegte Literatur, sind in dieser Arbeit genannt und aufgelistet. Die aus den Quellen wörtlich entnommenen Stellen, sind als solche kenntlich gemacht. Das Thema dieser Arbeit wurde von mir bisher weder im In- noch Ausland einer Beurteilerin/einem Beurteiler zur Begutachtung in irgendeiner Form als Prüfungsarbeit vorgelegt. Diese Arbeit stimmt mit der von den Begutachterinnen/Begutachtern beurteilten Arbeit überein.

Wien, 02.02.2024

Signature

Contents

1	Introduction	1
2	Technical Background	5
2.1	Basic Nuclear Magnetic Resonance (NMR) Principles	5
2.1.1	Magnetization	5
2.1.2	Excitation	6
2.1.3	Relaxation	8
2.1.4	Refocusing	9
2.1.5	Induction	9
2.1.6	Chemical Shift	10
2.1.7	X-Nuclei	12
2.2	Signal Modulation in MR	13
2.2.1	Relaxation Mechanisms	13
2.2.2	Inversion Recovery - T_1 Measurement	20
2.2.3	Hahn Spin-Echo - T_2 Measurement	21
2.3	Spatial encoding	23
2.3.1	Slice Selection	23
2.3.2	Frequency Encoding	23
2.3.3	Phase Encoding	24
2.3.4	k-space	25
2.4	Magnetic Resonance Spectroscopic Imaging (MRSI)	27
2.4.1	Phase-encoded MRSI	27
2.4.2	Spatial-spectral Encoded MRSI	29

2.5	Brain Metabolism	32
2.5.1	Positron Emission Tomography (PET)	34
2.5.2	Deuterium Metabolic Imaging (DMI)	34
3	Materials and Methods	37
3.1	Implementation of Inversion Recovery and Hahn Spin-Echo into CRT sequence	37
3.2	MR scanner	42
3.3	Radiofrequency coil	43
3.4	Deuterium Labeled Glucose	44
3.5	Measurement Protocol	45
3.6	Data Reconstruction	46
3.7	Spectral Fitting	47
3.8	Data Evaluation and Statistical Analysis	48
4	Results	49
4.1	Phantom	49
4.2	In vivo	53
4.2.1	Natural abundance Water	53
4.2.2	Orally administered deuterated Glucose	55
5	Discussion	61
6	Conclusion	65
	Bibliography	74
	List of Abbreviations	75
	List of Figures	78
	List of Tables	79

1 Introduction

The roots of modern Magnetic Resonance Spectroscopic Imaging (MRSI) go back to the early 1940s, marked by simultaneous but independent discoveries of Nuclear Magnetic Resonance (NMR) by Purcell et al. [1] and Bloch et al. [2], leading to their joint Nobel Prize in 1952. Initially employed by physicists to determine nuclear magnetic moments, the discovery of the chemical shift by Proctor and Yu [3] in 1950 laid the fundament for modern MR spectroscopy. Shortly afterward the first ^1H spectra of ethanol with separate peaks from methyl and methylene and hydroxyl protons were published by Arnold et al. [4] followed by first in vivo results of the rodent and human brain by Behar et al. [5] and Bottomley et al. [6], ultimately demonstrating the high potential of MRS techniques to explore static and dynamic aspects of the metabolism in physiology and pathophysiology [7]. Shortly after the introduction of in vivo Magnetic Resonance Imaging (MRI) in the early 1980s by Lauterbur [8] and Mansfield [9], acknowledged with the Nobel Prize in 2003, in vivo MR spectroscopic imaging (MRSI) was introduced by Brown et al. [10] and Mansfield [11]. Over the last 30 years, MRSI has undergone a remarkable evolution including signal enhancement through higher magnetic field strengths and innovative encoding methods for more efficient sampling of the k -space, ultimately leading to higher achievable spatial and temporal resolution. All this progress elevated MRSI into a robust and reliable method that allows non-invasive and non-ionizing mapping of various metabolites in animals and humans [12].

Recently Deuterium metabolic imaging (DMI) has proven to be a simple and robust Magnetic Resonance Spectroscopy technique (MRS) based on nuclear magnetic resonance (NMR) to non-invasively map the cellular glucose (Glc) uptake and downstream metabolism, e.g., in the human brain after oral or intravenous administration of non-invasive and safe deuterium labeled glucose. [^{18}F]-FDG-PET is the current clinical gold standard to detect cellular glucose uptake but requires invasive administration of radioactive tracers and does not give information about downstream metabolites due to glucose trapping in the cell. Since many severe brain pathologies feature regional differences in the brain glucose metabolism, there is a growing interest in a non-radioactive alternative approach to image glucose metabolism [13].

Administered non-ionizing deuterium labeled glucose is taken up by brain cells and incorporated into downstream products of the glucose metabolism, which can be dynamically and spatially resolved assessed using DMI. This allows a distinction of healthy oxidative from pathologic anaerobic pathways represented by oxidatively synthesized Glx and glycolitically synthesized lactate, respectively, which is not possible using [^{18}F]-FDG-PET [7, 13, 14].

In contrast to conventional ^1H MRS where water and lipid signals are orders of magnitudes higher than the signals of the metabolites of interest, natural abundance ^2H water and ^2H lipid signals detected with DMI are in the same range as administrated deuterium labeled compounds. Hence, no sophisticated water and lipid suppression methods are required and signal contamination from interfering compounds outside the field of view is minimized. The sparsity of acquired DMI spectra allows for simpler spectral quantification and additionally, a 6.5-fold lower Larmor frequency makes DMI less sensitive to magnetic field inhomogeneities compared to ^1H MRS. For ^2H resonances, quadrupolar relaxation mechanisms are dominant, while the contribution of dipolar relaxation effects are minimized. This leads to short spin-lattice (T_1) and spin-spin (T_2) relaxation times, which are relatively independent from the magnetic field strength B_0 and additionally allows for shorter repetition times (TR), ultimately reducing overall scan times compared to conventional ^1H acquisitions [7, 13].

To estimate metabolite concentrations accurately, tissue-specific T_1 and T_2 relaxation times of ^2H -Glc and ^2H -Glx would be desirable. However, to the best of our knowledge and with the exception of deuterated water [15], only unlocalized relaxation constants of deuterium resonances (e.g. Glc, Glx, Lac) have been reported [13, 16–18], as prolonged acquisition times of conventional MRSI sequences limit the achievable spatial resolution.

The aim of this master thesis is to measure tissue-specific T_1 and T_2 relaxation constants of deuterium resonances in gray and white matter. 3D ^2H -FID-MRSI sequence using hamming-weighted non-Cartesian concentric ring trajectory [19] sampling was modified to allow spatially resolved measurements of the T_1 and T_2 relaxation times. Therefore, Inversion time recovery and Hahn spin-echo acquisition schemes were implemented in the sequence in an interleaving manner. The developed sequence was employed on a 7T MR scanner and validated using a water phantom followed by in vivo measurements. Eight healthy volunteers were scanned to measure tissue-specific relaxation time constants of water, Glc and Glx after oral administration of deuterium labeled glucose.

2 Technical Background

2.1 Basic Nuclear Magnetic Resonance (NMR) Principles

This section aims to provide a basic overview of Nuclear Magnetic Resonance (NMR) principles, using the classical description, which provides the reader a more intuitive picture of the physical principles of NMR. This chapter mainly focuses on the book "In vivo NMR spectroscopy: principles and techniques" by De Graaf [7]. A full quantum mechanical description of NMR physics can be found in [20].

2.1.1 Magnetization

In classical mechanics, each rotating macroscopic object features an angular momentum, with the tendency to keep spinning. A corresponding property exists in subatomic particles such as electrons, neutrons, and protons which, despite not actually rotating, have an intrinsic angular momentum called spin. Each particle featuring a spin inherently possesses a magnetic moment $\vec{\mu}$. It should be noted that spin and magnetic moments are used synonymously in NMR literature.

Without an external magnetic field, the magnetic moments of a sample are randomly oriented, and thus no macroscopic magnetization can be observed, as shown in figure 2.1a,b. However, when the sample is placed in a magnetic field, the magnetic moments start precessing, due to their intrinsic angular moment, with a spe-

cific frequency, defined by the type of nuclei. This was labeled Larmor frequency ν_0 (MHz) (figure 2.1c) and is independent of the spin orientation but proportional to the external magnetic field strengths given by

$$\nu_0 = \frac{\omega_0}{2\pi} = \frac{\gamma}{2\pi} B_0, \quad (2.1)$$

where γ is the gyromagnetic ratio ($\text{rad}\cdot\text{MHzT}^{-1}$) and B_0 is the magnetic field strength (T).

Molecular tumbling and Brownian motion of neighboring spins can cause local magnetic field fluctuations, perturbing the spin orientation when matching the Larmor frequency. These not completely random perturbations lead to a distribution that slightly favors a parallel spin orientation to the direction of the external magnetic field \vec{B}_0 (here defined as z -direction), resulting in a macroscopic net magnetization vector \vec{M} , illustrated in figure 2.1d. It is important to mention that the spin distribution in the transverse (x,y -plane) is still random and also the net magnetization is built up only by a small proportion of spins (parts per million) biased towards a parallel orientation. The net magnetization will exponentially build up in a specific time which depends on nucleus type and molecular environment and is defined as longitudinal relaxation (see section 2.1.3). The net magnetization eventually converges to a longitudinal equilibrium magnetization M_0 which can be calculated from the Boltzmann distribution:

$$M_0 = \frac{N\gamma^2 h^2 B_0}{16\pi^2 k_B T}, \quad (2.2)$$

with N being the number of spins, h the Plank's constant, k_B is the Boltzmann constant and T the Temperature [7].

2.1.2 Excitation

A second cosine modulated magnetic field \vec{B}_1 , perpendicular to the static field \vec{B}_0 and oscillating at the Larmor frequency of the target nuclei in the sample ν_0 , can be used to flip the net magnetization towards the transverse plane where it can be

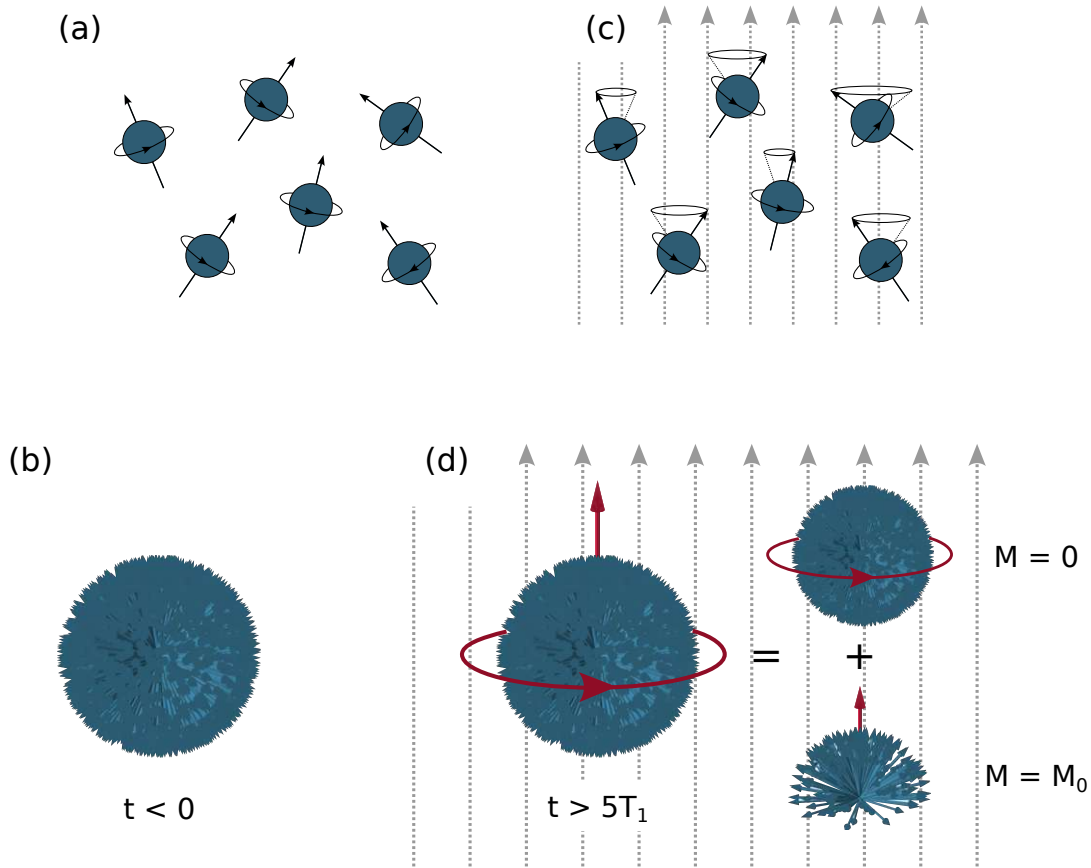


Figure 2.1: Without an external magnetic field, spins are randomly distributed (a), preventing the formation of a macroscopic net magnetization. If all spins are placed at the origin of the coordinate system, the randomly distributed spins can be visualized as a "spin-orientation" sphere (b). Spins perceiving an external magnetic field \vec{B}_0 precess along the axis of the field with their specific Larmor frequency (c), which can be simplified as a precessing spin-orientation sphere. Over time, molecular tumbling and Brownian motion are causing a small population of spins in the order of parts per million to slightly favor a more parallel orientation towards the direction of \vec{B}_0 , and building up a net magnetization M_0 although the majority of the spins are randomly distributed (d).

measured, figure 2.2a. The magnetic field \vec{B}_1 with a field strength of typically five to six orders of magnitude smaller compared to the static B_0 field strength, creates a constant torque that deflects the entire rotating spin distribution including the net magnetization vector from the z -axis towards the transverse xy -plane in a specific angle, defined as the flip angle. The flip angle can be adjusted using the amplitude and duration of the Radio-Frequency (RF) pulse creating \vec{B}_1 . This process is generally defined as excitation with typically 90° flip angle or below, while using a 180° flip angle is defined as inversion [7].

2.1.3 Relaxation

Longitudinal Relaxation

Upon excitation or any other perturbations, the spin population endeavors to return to the thermal equilibrium state see figure 2.2b. The reappearance of a net magnetization M_z along the z -axis is called longitudinal relaxation or spin-lattice relaxation and can be described by:

$$M_z(t) = M_0 - (M_0 - M_z(0))e^{-t/T_1}, \quad (2.3)$$

with $M_z(0)$ being the longitudinal magnetization at time zero and T_1 the exponential relaxation time constant [7, 21].

Transversal Relaxation

After flipping the net magnetization towards the transversal plane all spins initially feature a coherent phase, which dephase over time via random local field fluctuations generated by Brownian motion and molecular tumbling ultimately leading to an irreversible disappearance of the detectable macroscopic transverse magnetization. This effect is called transversal or spin-spin relaxation, see figure 2.2b and is characterized by an exponential decay:

$$M_{xy}(t) = M_{xy}(0) \cdot e^{-\frac{t}{T_2}}. \quad (2.4)$$

where T_2 is the exponential time constant of the decay of the detectable magnetization. Additionally, static magnetic field inhomogeneities caused by the sample itself, lead to an accelerated decay of the transverse net magnetization, described by the relaxation constant T_2^*

$$T_2^* = T_2 + T_2' \quad (2.5)$$

where T_2' is the exponential signal decay constant of static inhomogeneities.

2.1.4 Refocusing

Since static magnetic field inhomogeneities causing T_2' relaxation are time-invariant, dephasing of the spins can be reversed using an 180° RF pulse, creating a so-called spin-echo after a defined time delay (TE , echo time). After initial excitation and a time delay of $TE/2$, spins are flipped by 180° around the x - or y -axis, leading to re-phasing of the spins and spin-echo formation after another $TE/2$ time delay [7].

2.1.5 Induction

After excitation, spins precessing in the xy -plane (in a rotating frame of reference) and featuring a coherent phase create a detectable electrical signal in a nearby receiver coil, via electromagnetic induction according to Faraday's law. The detected oscillating signal decays exponentially with T_2^* and is defined as Free Induction Decay (FID), see figure 2.2c. The FID can be described using a complex function where the real part (M_x) represents the absorption and the imaginary part (M_y) the dispersion. In reality, the FID is a superposition of multiple frequencies (due to chemical shifts, see section 2.1.6) from different compounds which makes it difficult to distinguish between different metabolites in the time domain. Applying a Fourier transform (FT) converts the signals into the frequency domain which

will result in a frequency spectrum with different peaks corresponding to different chemical compounds [7].

2.1.6 Chemical Shift

According to equation 2.1 the Larmor frequency only depends on the gyromagnetic ratio γ and the field strength of the external magnetic field B_0 . However, in 1950 Proctor and Yu [3] discovered two different resonance frequencies for ^{14}N within an ammonium nitrate solution. This observed phenomenon that the chemical environment of a nucleus causes small local variations in magnetic resonance frequencies was labeled chemical shift. The nucleus is surrounded by an electronic cloud, creating an opposing magnetic field that shields it from the external magnetic field. This reduces the effective magnetic field perceived by the nucleus, resulting in a lower Larmor resonance frequency. Additionally, atoms with higher electronegativity pull the electron cloud away from protons, decreasing electronic shielding and leading to a higher resonance frequency.

While the Larmor resonance frequencies are expressed in Hertz (Hz), the chemical shift is commonly expressed in parts-per-million (ppm) relative to a reference compound:

$$\delta = \frac{\nu - \nu_{\text{ref}}}{\nu_{\text{ref}}} \times 10^6, \quad (2.6)$$

where δ is the chemical shift, ν and ν_{ref} are the Larmor frequencies of the compound of interest and the reference compound, respectively. Using ppm has the advantage of expressing chemical shifts independent of B_0 which makes a comparison of results between laboratories using different magnetic field strengths more feasible.

The discovery of the chemical shift was revolutionary and formed the basis for in vivo magnetic resonance spectroscopy (MRS) as frequency spectra allow for simultaneous non-invasive analysis of different chemical compounds and can provide valuable information about metabolite concentrations in tissue, e.g., in the brain see figure 2.3 [7].

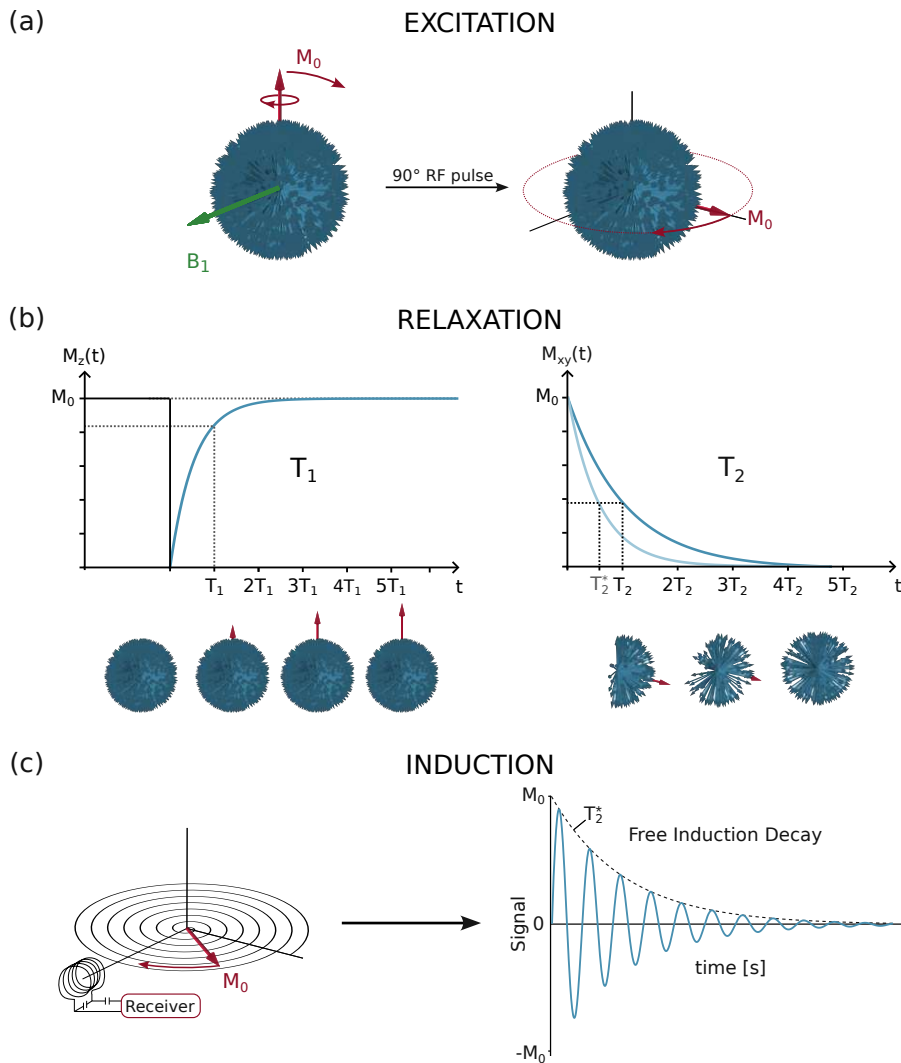


Figure 2.2: The net magnetization is flipped to the transversal plane where it can be measured using a 90° RF pulse (a). The spins will try to get back to an equilibrium state. Longitudinal relaxation describes the reappearance of the net magnetization along the z -axis, whereas transversal relaxations leads to dephasing of the spins due to local field fluctuations resulting in a loss of the transversal magnetization (b). In the rotating reference frame, the net magnetization will precess in the transversal plane after excitation, inducing a signal in a nearby receiver coil, which is called Free Induction Decay (FID) (c).

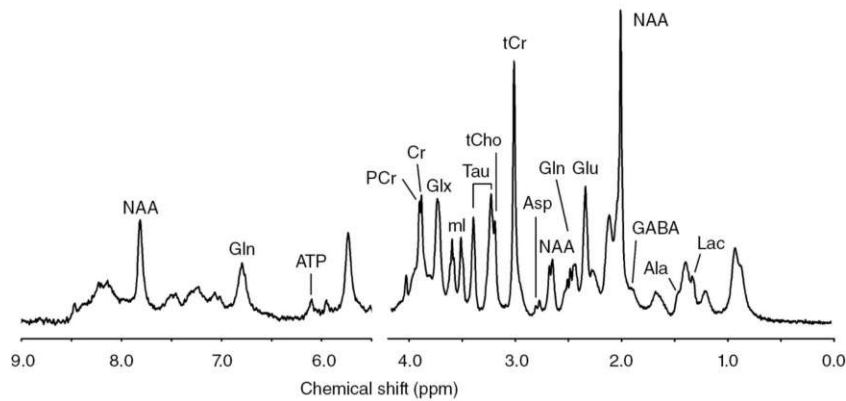


Figure 2.3: Exemplary ^1H MRS spectrum of a rat brain in vivo which shows the separation of peaks corresponding to different metabolites due to the chemical shift. Figure taken from [7].

2.1.7 X-Nuclei

Hydrogen is highly abundant in living tissue, and commonly present in the majority of metabolites. Therefore ^1H magnetic resonance spectroscopy is commonly used for in vivo experiments, providing high sensitivity and numerous detectable metabolites, but the acquisition is not unproblematic as signals of metabolites are several orders of magnitude lower compared to tissue water or fat signal and sophisticated water and fat suppression is needed [7].

Besides ^1H it is also possible to measure other MR-sensitive nuclei possessing a nuclear spin, most commonly used are ^2H , ^{13}C , ^{17}O , ^{31}P or ^{23}Na . Non-hydrogen or non-proton magnetic resonance spectroscopy is defined as X-nuclei spectroscopy, which offers valuable and complementary insights into important processes, e.g., cellular energy metabolism and allows for establishing connections to pathological conditions such as neurodegenerative diseases [22, 23].

However, X-nuclei MRS generally features lower intrinsic detection sensitivity as a result of lower gyromagnetic ratios leading to a lower signal-to-noise ratio (SNR) compared to conventional ^1H MRS [24]. This can be compensated by increasing the magnetic field strength, e.g., by using ultra-high field MR scanners offering a

significant SNR gain [25]. Deuterium metabolic imaging is a re-discovered X-nuclei MRS modality, which gained recent attention [13, 16, 26]. It offers non-invasive insight into glucose metabolism and can differentiate between normal oxidative and pathologic glycolytic pathways using deuterium labeled glucose as non-invasive and harmless tracer as discussed in more detail in Chapter 2.5.2.

2.2 Signal Modulation in MR

Until now we only discussed the fundamental basics of NMR physics including longitudinal and transversal relaxation. This chapter tries to give a more detailed description of the main mechanisms that lead to relaxation and how T_1 and T_2 relaxation time constants can be measured using Inversion recovery and Hahn spin-echo acquisition schemes.

2.2.1 Relaxation Mechanisms

Dipolar relaxation is the dominant relaxation effect for nuclei featuring spin quantum number I of $1/2$ as described by Bloembergen, Purcell and Pound (BPP) in 1948 [27] and further developed by Solomon [28]. In case of nuclei with spin quantum numbers $I \geq 1$, other relaxation mechanisms can dominate e.g., quadrupolar relaxation effects in case of deuterium ^2H , or chemical shift anisotropy effects in case of ^{31}P .

As a detailed mathematical description of relaxation mechanism exceeds the scope of this thesis, interested readers are referred to [20], which provides a detailed description of dipolar and quadrupolar relaxation mechanisms. Detailed explanations of relaxation mechanisms can also be found in books by Levitt [21] and Kowalewski [29].

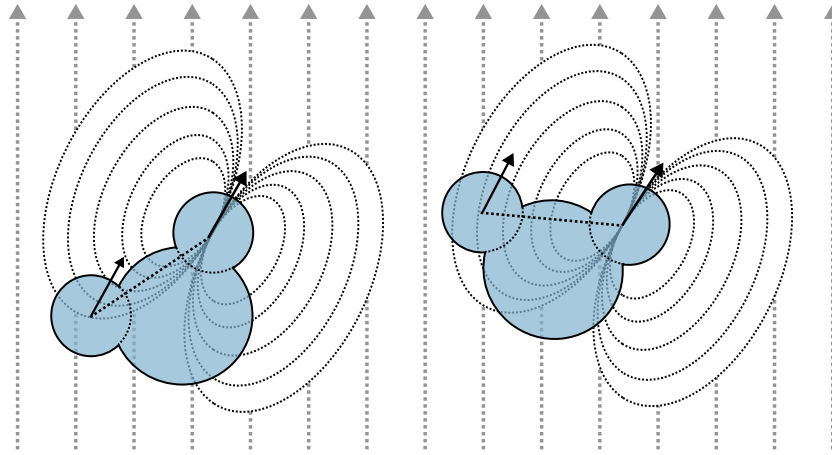


Figure 2.4: One proton within a water molecule feels the magnetic field generated by the other proton. Due to Brownian motion and molecular tumbling the molecule rotates and transits randomly in the external magnetic field B_0 (parallel gray lines) which causes randomly fluctuating magnetic fields leading to relaxation.

Magnetic dipolar-dipolar Relaxation

Each spin can be visualized as a dipolar magnetic moment, interacting with the magnetic field of neighboring spins. Brownian motion and molecular tumbling will lead to randomly fluctuating magnetic fields perturbing the local field of other nearby spins, see figure 2.4.

Relaxation is induced when the fluctuation frequency of the local magnetic fields approaches Larmor frequency.

The autocorrelation function characterizes frequency components of the local magnetic field over time:

$$G(\tau) = \langle B_{\text{loc}}(t)B_{\text{loc}}(t + \tau) \rangle = \langle B_{\text{loc}}^2 \rangle e^{-|\tau|/\tau_c} \neq 0, \quad (2.7)$$

with τ_c being the correlation time of the fluctuations, which is in the range of $10^{-12} - 10^{-10}$ s for mobile magnetic moments in a liquid. High correlation is expected for short delays of τ , whereas the influence of Brownian motion and molecular tumbling leads to low correlation for larger delays, reflecting the exponential nature of the correlation function. The spectral density function $J(\nu)$ is

the Fourier transform of the correlation function:

$$J(\nu) = \langle B_{\text{loc}}^2 \rangle \frac{\tau_c}{1 + 4\pi^2\nu^2\tau_c^2}. \quad (2.8)$$

Rapidly fluctuating magnetic fields are characterized by short correlation times τ_c and broad spectral density functions [7, 21].

We have now discussed how local magnetic fields can perturb the orientation of nuclear spins in a classical view. Bloembergen, Purcell and Pound (BPP) [27] were the first to accurately describe dipole-dipole relaxation in liquids, which was later adapted by Solomon [28], both using quantum mechanics to describe the transition probabilities between spin states and the local magnetic fields.

In the quantum mechanical approach energy states, momentum and other systematic properties are described using discrete values. Without an external magnetic field (\vec{B}_0) energy levels of the spins are equal. Applying a magnetic field lifts the degeneracy:

$$\Delta E = \gamma\hbar B. \quad (2.9)$$

This effect is called Zeeman Effect and will lead to a two-level system in the most simplified case, corresponding to spins parallel (α) or antiparallel (β) to \vec{B}_0 . If the RF pulse matches Larmor frequency, transitions between the energy states are possible. This brief description of quantum NMR principles is sufficient for the following description of dipolar relaxations, a more detailed description can be found in [7, 20].

A homonuclear two-spin system featuring four energy eigenstates and three transition types with a transition probability W depending on the frequency components of the local magnetic field, see figure 2.5. W_1 describes the probability of one spin flipping while leaving the other one unperturbed. A zero-quantum transition is described by W_0 , where both spins flip in opposite directions while a double-quantum transition W_2 occurs when both spins flip in the same direction [7]. The

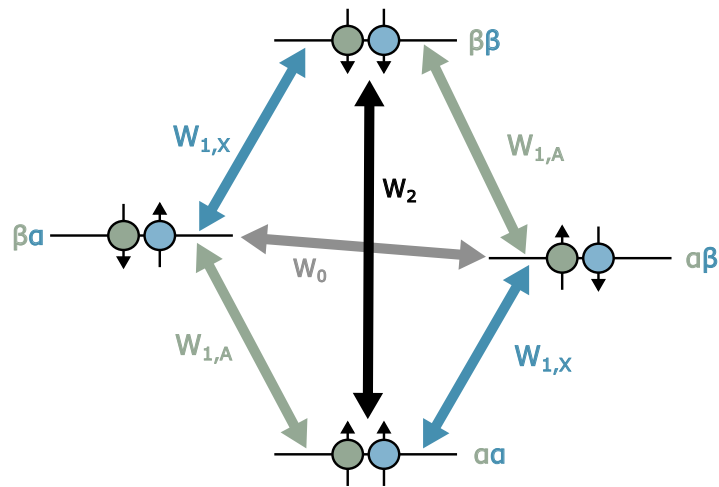


Figure 2.5: Energy diagram of a dipolar-coupled two-spin state system. There are three different transition probabilities. While the single quantum transition W_1 changes the energy levels, W_0 and W_2 correspond to single- and double-quantum transitions where both spins flip in opposite and the same direction, respectively, at the same time.

transition probabilities can be linked to the spectral density $J(\nu)$ as follows:

$$\begin{aligned}
 W_0 &= \frac{1}{10} C_1^2 J(0) \\
 W_1 &= \frac{3}{20} C_1^2 J(\nu) \\
 W_2 &= \frac{3}{5} C_1^2 J(2\nu)
 \end{aligned} \tag{2.10}$$

with $C_1^2 = \frac{\mu_0}{8\pi^2} \frac{h\gamma^2}{r^3}$.

Solomon [28] then connected the transition probabilities to T_1 and T_2 relaxation constants:

$$\frac{1}{T_1} = \frac{3}{10} C_1^2 (J(\nu) + 4J(2\nu)) \tag{2.11}$$

$$\frac{1}{T_2} = \frac{3}{20} C_1^2 (3J(0) + 5J(\nu) + 2J(2\nu)) \tag{2.12}$$

T_1 and T_2 relaxation scale inversely with the square of the gyromagnetic ratio and both depend on frequency components at the Larmor frequency and twice the Larmor frequency. However, only T_2 relaxation is affected by low-frequency components. This implies that the transverse relaxation is very small for slow molecular tumbling (i.e. water bound to macromolecular structures or water in ice) [7]. As visible in figure 2.6, T_1 and T_2 are equal for short correlation times τ_c (small molecules and non-viscous liquids) also known as the extreme narrowing limit ($\nu^2\tau_c^2 \ll 1$). With increasing correlation time the function of T_1 reaches a minimum, while T_2 continuously decreases [21].

The dipole-dipole interaction model of Bloembergen, Purcell and Pound predicts increasing T_1 relaxation constants, but independent T_2 relaxation with increasing magnetic field strength for relaxation effects solely dominated by dipolar-dipolar interaction [7]. However, in contradiction to the BPP theory decreasing T_2 values were observed in most tissues at high magnetic field strength at ≥ 7 T, according to [30], attributed to dynamic dephasing effects due to local macro- and microscopic magnetic field inhomogeneities, which are linearly increasing with B_0 .

Electric quadrupole interactions

Nuclei with a spin quantum number of $I \geq 1$ have a non-spherically symmetric electric charge distribution in contrast to nuclei with spin $I = 1/2$ (e.g. ^1H). As a result, interactions between the quadrupole moment of the nuclei and electric field gradients generated by surrounding electron clouds become orientation-dependent. Since the quadrupolar interaction is usually much stronger than any other interactions, it is the dominant relaxation mechanism in nuclei with $I \geq 1$ e.g. ^2H , ^{17}O , ^{39}K resulting in relaxation time constants in the order of milliseconds [7, 13, 16, 21, 29].

Quadrupolar relaxation times of deuterium are characterized by [20, 31]:

$$\frac{1}{T_{1,Q}} = \frac{3}{80} \left(\frac{e^2qQ}{\hbar} \right)^2 \left(1 + \frac{\eta^2}{3} \right) (J(\omega) + 4J(2\omega)) \quad (2.13)$$

$$\frac{1}{T_{2,Q}} = \frac{1}{160} \left(\frac{e^2qQ}{\hbar} \right)^2 \left(1 + \frac{\eta^2}{3} \right) (9J(0) + 15J(\omega) + 6J(2\omega)), \quad (2.14)$$

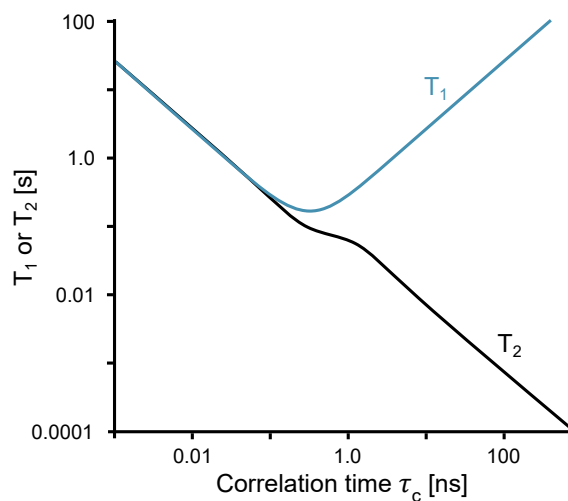


Figure 2.6: T_1 and T_2 dipolar relaxation as a function of the correlation time τ_c : In the extreme narrowing limit (gases and small molecules in water) $T_1 = T_2$. For larger molecules, viscous liquids and solids corresponding to larger correlation times τ_c : $T_1 \gg T_2$

with e^2qQ/\hbar being the quadrupolar coupling constant (QCC), Q is the nuclear quadrupole moment (e.g. ^2H has a small Q of $2.9 \cdot 10^{-31} \text{ m}^2$), η the electrical field gradient asymmetry parameter and $J(\omega)$ the spectral density function at Larmor frequency ω .

In the extreme narrowing regime ($\tau_c^2\omega^2 \ll 1$) $J(2\omega) = J(\omega) = J(0)$ are equal to $2\tau_c$ and equation 2.15 simplifies to:

$$\frac{1}{T_{1,Q}} = \frac{1}{T_{2,Q}} = \frac{3}{8} \left(\frac{e^2qQ}{\hbar} \right)^2 \left(1 + \frac{\eta^2}{3} \right) \tau_c. \quad (2.15)$$

Chemical shift anisotropy

The chemical shift (discussed in section 2.1.6) is, in reality, dependent on the orientation of the molecule relative to the main magnetic field \vec{B}_0 . The orientation-dependent chemical shift in the liquid state is effectively averaged due to rapid molecular motion. However, nuclei perceive magnetic field fluctuations generated by molecular tumbling and introducing an additional pathway for relaxation. In

relaxation processes affected by chemical shift anisotropy, T_1 and T_2 are not equal in the extreme narrowing limit and are proportional to the square of the main magnetic field strength. This effect is more pronounced with higher magnetic field strengths. In contrast to dipole-dipole relaxation, relaxation times that are dominated by chemical shift anisotropy mechanisms are inversely proportional to increasing magnetic field strengths B_0 . For example, in ^{31}P MRS dipolar and chemical shift anisotropy are the two main relaxation mechanisms. Depending on which effect is dominating, T_1 relaxation times will either increase or decrease with increasing magnetic field strength [7].

Spin rotation interaction

Coherent rotational motion of entire molecules, which can couple with the spin of the nucleus, can generate a magnetic field at the nucleus. Relaxation can be induced when this coupling is, for example, interrupted by collisions. Spin rotation relaxation is most pronounced in small, symmetric molecules with short correlation times. However, this mechanism holds minimal relevance for the majority of molecules studied using in vivo NMR [7].

Scalar coupling

Besides dipole-dipole interactions, two nuclear spins can also couple indirectly via electrons in a chemical bond, resulting in splitting of resonances into several smaller peaks. This effect is called scalar coupling or J coupling and can only be described with quantum mechanics. Without interaction, nuclear and electron spins energetically favor antiparallel constellation. However, when two nuclei are covalently bound, their electrons must have an antiparallel orientation due to the Pauli exclusion principle, which forbids two identical particles occupying the same quantum mechanical state. The nuclear spins can still be in parallel or antiparallel orientation to each other, but antiparallel orientation is energetically favored since both nuclear and electron spin are also in antiparallel orientation to each other, while for parallel nuclear spin constellation one nuclear-electron spin pair is forced to be parallel. As a result of the scalar coupling, the single resonances of the two

nuclei are split up into two peaks with half intensity corresponding to two different frequencies.

Relaxation induced by scalar coupling can be described by considering a two-spin system. The magnetic field produced by spin A will act indirectly on spin B and vice versa. Relaxation of spin B can be induced if the coupling constant becomes time-dependent, which is the case for exchange processes (e.g. two nuclei exchanging positions) or relaxation of spin A. These two processes are called scalar relaxation of first and second kind [7].

2.2.2 Inversion Recovery - T_1 Measurement

Inversion recovery is commonly used to measure the longitudinal relaxation time constant T_1 due to its robustness and accuracy but comes at the cost of long acquisition times, as the longitudinal magnetization after excitation should preferably be fully relaxed, leading to long repetition times (TR). After initial inversion of the net magnetization using a 180° RF pulse the inverted magnetization increases exponentially towards the positive z -axis with T_1 time constants. Partially relaxed longitudinal magnetization is then flipped in the transversal plane using 90° excitation, followed by signal acquisition, see figure 2.7. By varying the delay between inversion and excitation pulse (defined as inversion time TI), the longitudinal relaxation T_1 can be approximated according to equation 2.3 with $M_z(0) = -M_0$ for a perfect inversion pulse. To achieve a full 180° inversion is not always possible due to B_1 inhomogeneities in the sample, especially at ultra-high magnetic field strengths, therefore a three-parameter fit is more commonly used to obtain the longitudinal relaxation time T_1 [7]. For an improved fit, it is recommended to use repetition times TR at least 3 times greater than the expected T_1 , to ensure sufficient longitudinal recovery towards the thermal equilibrium before the next inversion pulse [32].

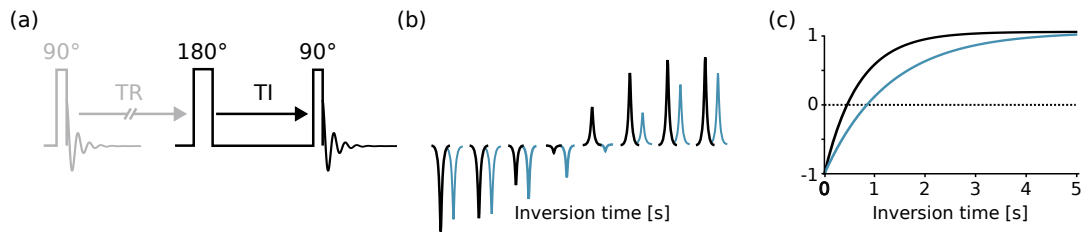


Figure 2.7: Measuring T_1 relaxation with Inversion recovery: The net magnetization vector is inverted by a 180° pulse followed by a 90° pulse which flips the magnetization in the transverse plane. The variable delay between these two pulses is called inversion time TI (a). For short inversion times, the magnetization is negative (nearly no relaxation) and becomes positive (relaxation back to equilibrium) for longer TI (b). The longitudinal relaxation time constant can be estimated by a three-parameter fit (c).

2.2.3 Hahn Spin-Echo - T_2 Measurement

The transverse relaxation time T_2 can be measured using the Hahn spin-echo method, which was first proposed by Erwin Hahn [33] in the 1950s and modified by Carr and Purcell in 1954 [34]. After flipping the net magnetization towards the transversal plane using a 90° pulse, spins dephase due to T_2^* relaxation. As mentioned in 2.1.4, a refocusing pulse flips the entire spin ensemble by 180° after a delay of $TE/2$ forming a spin-echo after another time delay of $TE/2$, see figure 2.8d. Effects of T_2 relaxation can not be recovered by the Hahn-spin echo acquisition scheme, hence with increasing echo times signals decay exponentially according to equation 2.4 [7].

At the beginning of NMR experiments excitation and refocussing pulses were applied along the same axis. However, imperfect 180° pulses and time-dependent magnetic field inhomogeneities lead to shorter measured T_2 values [29]. In 1958 Meiboom and Gill changed the phase of the refocussing pulse by 90° relative to the excitation pulse leading to more accurate transversal relaxation times. This method is now known as the CPMG sequence (Carr-Purcell-Meiboom-Gill) [34, 35].

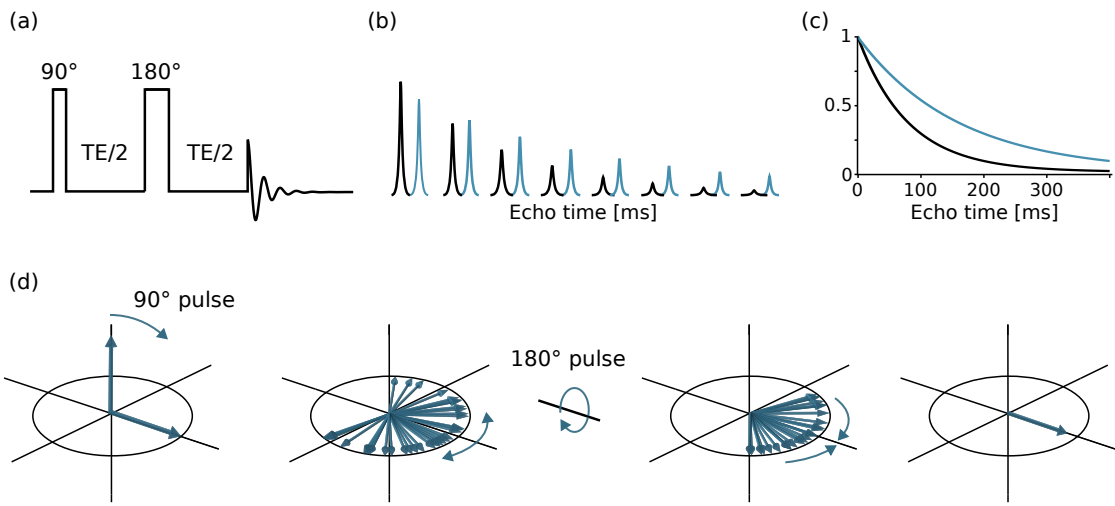


Figure 2.8: Measuring T_2 relaxation with Hahn spin-echo: After excitation, the spins start dephasing in the transversal plane because of T_2^* relaxation. After $T_E/2$ the spins ensemble is flipped using a refocusing pulse, which results in rephasing of the spins and a spin-echo after $T_E/2$ (a). The acquired signal decays exponentially (b) and transversal relaxation constants can be obtained by exponential fitting (c). Illustration of dephasing and rephasing of the spins during Hahn spin-echo sequence (d).

2.3 Spatial encoding

To allow the detection of localized NMR signals, MR signals can be spatially encoded using three orthogonal coils generating magnetic field gradients in x -, y -, and z -direction (G_x , G_y , G_z), which are superimposed with the main magnetic field \vec{B}_0 . The localization techniques described in this section form the basis of MR imaging (MRI), which was developed in the 1970s by Mansfield [9] and Lauterbur [8] who later shared the Nobel Prize in Medicine in 2003.

2.3.1 Slice Selection

Applying a magnetic field gradient along the z -axis will alter the resonance frequency of the nuclei

$$\nu(r) = \frac{\gamma}{2\pi} B_0 + \frac{\gamma}{2\pi} rG, \quad (2.16)$$

where G is a magnetic field gradient in z -direction. Simultaneously applying a magnetic field gradient along with an RF pulse, allows to selectively excite spins resonating within the bandwidth of the RF pulse, which is defined as slice selection. The thickness of the slice is determined by the amplitude of the magnetic field gradient and the bandwidth of the RF pulse. A stronger magnetic field gradient (corresponds to the slope in figure 2.9) or a smaller bandwidth of the RF pulse both result in the selection of a thinner slice, as illustrated in figure 2.9. Following slice selective excitation, the signal can be further encoded in the other two spatial dimensions using frequency and phase encoding [7].

2.3.2 Frequency Encoding

When a frequency encoding gradient is turned on during data acquisition, the MR signal will become position-dependent, i.e., spins precess with different Larmor frequencies along the direction of gradient field. The acquired signal comprises mul-

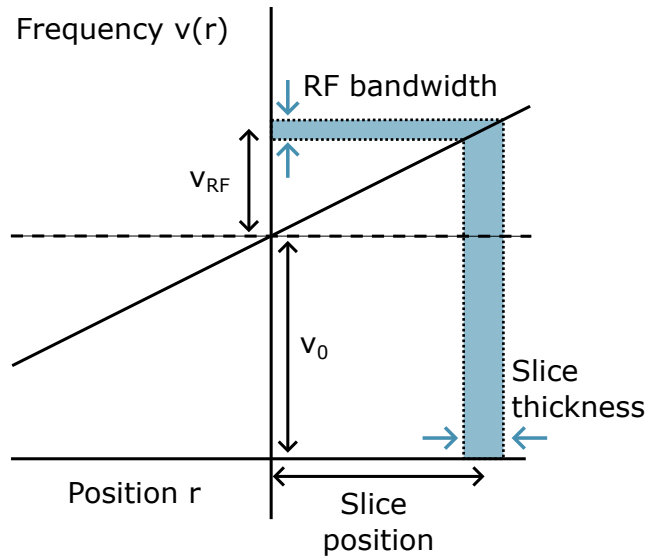


Figure 2.9: In the presence of a magnetic field gradient G , the Larmor frequency becomes linearly dependent on G . A slice can be selected by simultaneously applying an RF pulse and magnetic field gradient.

multiple signals originating from various regions of the sample. Different frequencies can be directly converted to spatial positions along the direction of the frequency encoding gradient G_x [7].

2.3.3 Phase Encoding

To spatially encode the third dimension, a phase-encoding gradient is used, employed with a specific amplitude and duration between excitation and acquisition, creating different positions depending Larmor frequencies along the direction of the gradient. After the gradient is turned off, spins precess again with similar Larmor frequencies but feature incoherent phases along the phase-encoding direction. These phase differences are linearly proportional to the gradient amplitude and duration, corresponding to an indirect frequency

$$\nu = \frac{1}{2\pi} \frac{d\phi}{dt}. \quad (2.17)$$

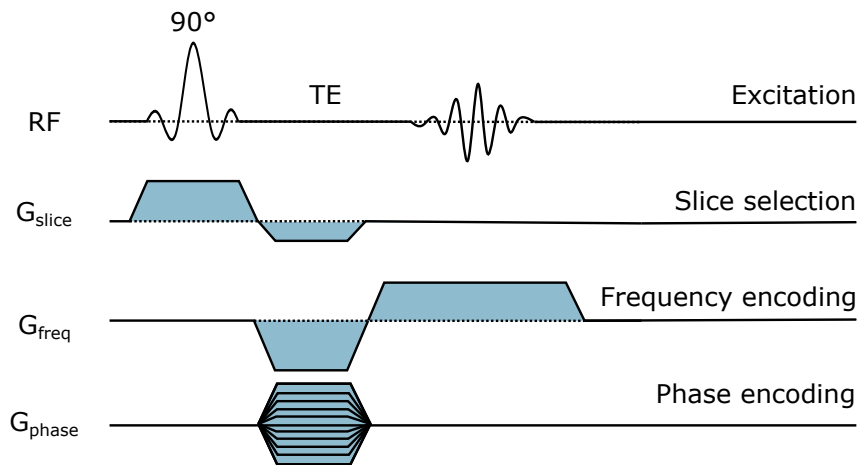


Figure 2.10: A slice is selected by simultaneous application of an RF pulse and a magnetic field gradient G_{slice} . Spatial encoding along the other two dimensions is accomplished through the use of frequency encoding G_{freq} and phase encoding G_{phase} gradients. By incrementing the phase encoding gradient and activating a frequency encoding gradient during readout, k -space can be sampled along horizontal lines.

Through linearly incrementing the phase-encoding gradient, the phase of the signal is dependent on the position along the phase-encoding gradient.

In general, spatial encoding using G_x, G_y and G_z gradients is performed for each TR and repeated multiple times, depending on the desired spatial resolution, see figure 2.10. Hence, to fully sample an image with 32x32 in-plane resolution, 32 phase encoding steps are required, i.e., 32 repetitions. The acquired data is stored in a 2D matrix defined as k -space, which is further explained in more detail in the next section. The final 2D image is derived through a 2D Fourier transform [7].

2.3.4 k -space

The relationship between the MR image and MR signal can be described with the concept of k -space, which connects the frequency domain (k -space) with the image

space via a Fourier transformation.

The transverse magnetization M_{xy} is dependent on the magnetic field gradient $G(t)$ and can be expressed as follows

$$M_{xy}(G(t)) = M_x(G(t)) + iM_y(G(t)) = \int_{-\infty}^{\infty} M_0(r) e^{+i\gamma r \int_0^t G(t') dt'} dr, \quad (2.18)$$

where $M_0(r)$ is the spin density at position r . With the spatial frequency variable $k(t)$

$$k(t) = \gamma \int_{-\infty}^{\infty} G(t') dt' = \gamma Gt \quad (2.19)$$

equation 2.18 simplifies to

$$M_{xy}(k(t)) = \int_{-\infty}^{\infty} M_0(r) e^{ik(t)r} dr. \quad (2.20)$$

The detected MR signal $M_{xy}(k(t))$ in equation 2.20 is connected to the spatial spin density distribution $M_0(r)$ via an inverse Fourier transformation.

Similarities can be observed between equation 2.19 and the acquired phase of a spin in the presence of a gradient G_A at position r

$$\phi_A(r, t) = \gamma r \int_0^t G_A(t') dt', \quad (2.21)$$

Hence, $k(t)$ can be interpreted as frequency/phase of a spin at a unit distance, i.e., turning frequency- and phase encoding gradients on and off, can be visualized as moving through k -space along a trajectory.

Each point in k -space contains information about all points in image space and vice versa. While low spatial frequency components, which contain information on the overall shape and signal intensity of the image, are located in the extended k -space center, high spatial frequencies, containing information about contrast, are located in the periphery of the k -space. Moreover, the field of view (FOV) is inversely proportional to the distance between two discrete k -space points $\Delta k = 2\pi/\text{FOV}$ [7].

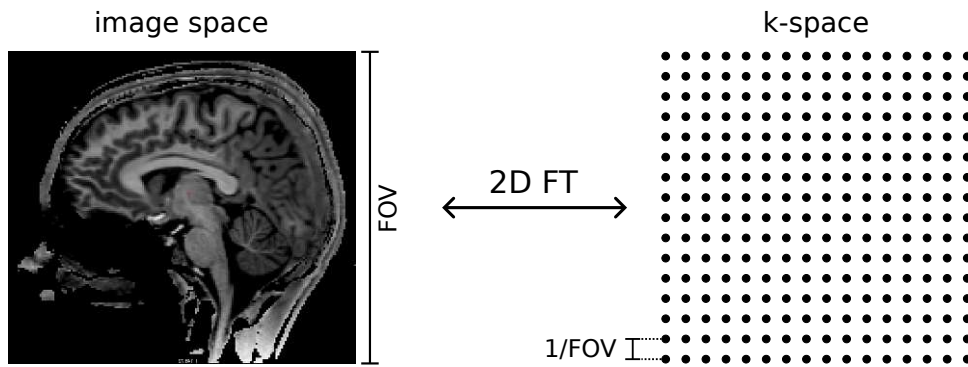


Figure 2.11: Image (left) and frequency domain (right) are connected via Fourier Transformation. Each point in k -space contains information about every point in image space and vice versa.

2.4 Magnetic Resonance Spectroscopic Imaging (MRSI)

Developed in the early 1980s [10, 11, 36] Magnetic Resonance Spectroscopic Imaging (MRSI) combines magnetic resonance spectroscopy with spatial encoding methods enabling non-invasive mapping of various metabolites in animals and humans [12]. By encoding another spatial dimension using e.g., phase encoding, it is possible to acquire localized spectra for each voxel, providing spatially-resolved information about the concentrations of different metabolites [7].

This section provides an overview of traditional phase-encoding MRSI as well as spatial-spectral encoding using non-cartesian concentric ring trajectories (CRTs), which were used to measure tissue-specific relaxation times in this thesis.

2.4.1 Phase-encoded MRSI

In contrast to MRI, where one spatial dimension is determined using frequency encoding, i.e., applying a gradient during readout, conventional magnetic resonance spectroscopic imaging (MRSI) uses phase-encoding gradients for all three spatial

dimensions. This ensures that frequency differences in the acquired signal correspond to chemical shifts of the metabolite and not to spatial positions. [37].

After an RF excitation pulse, each point in k -space is sampled separately by using three orthogonal gradients (G_x , G_y and G_z), as depicted in figure 2.12. By gradually incrementing the gradients per repetition time (T_R) each point is characterized by a gradient-induced phase-shift according to equation 2.19 and 2.21 [38]. This will extend the k -space by another dimension (three spatial, one FID time domain). Following data acquisition, spatially resolved spectra can be obtained by transforming the spatially encoded FID signals using spectral and spatial Fourier transformations:

$$s(k_x, k_y, k_z, t) \xrightarrow{\text{spectral FT}} F(k_x, k_y, k_z, \omega) \xrightarrow{\text{spatial FT}} f(x, y, z, \omega).$$

Fully sampled 3D MRSI features very long measurement times, especially for high resolutions. For instance, the total measurement time of a $16 \times 16 \times 16$ matrix with a T_R of 1.5 s would already be $T_{\text{meas}} = 16 \times 16 \times 16 \times 1.5 \cong 100$ min. Consequently, achieving higher spatial resolutions with traditional 3D phase-encoding sequences is constrained by long scanning times [37, 38].

This led to the development of different techniques to accelerate MR spectroscopic imaging. In general, shorter scanning times can be achieved by shortening the repetition time (T_R), but depending on the longitudinal relaxation times, this will decrease achievable SNR due to partial saturation of the magnetization. Other techniques to reduce overall scan times are spatial-spectral encoding methods, i.e., acquisition of multiple k -space points per (T_R), using non-cartesian readout trajectories to sample the k -space more efficiently, k -space undersampling or incorporating prior knowledge into data reconstruction. Covering all these different techniques exceeds the scope of this thesis. In the next chapter, only spatial-spectral encoding using non-cartesian ring trajectories (CRT), as it was used during the work of this thesis, will be discussed in more detail; information about different techniques to accelerate MR spectroscopic imaging can be found in [12].

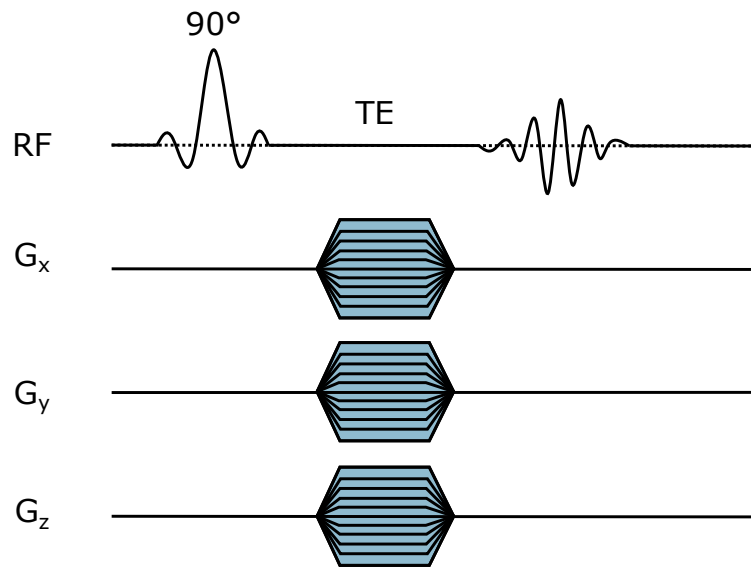


Figure 2.12: Schematic illustration of 3D CSI sequence: After excitation, the three orthogonal magnetic field gradients (G_x , G_y and G_z) are gradually incremented, which allows sampling of each point in k -space separately.

2.4.2 Spatial-spectral Encoded MRSI

Conventionally, k -space is sampled line-by-line on a rectangular Cartesian grid, which is required by using a fast Fourier transform (FFT) during image reconstruction. Alternatively, it is also possible to acquire k -space points along non-Cartesian trajectories such as spirals [39–41], radial trajectories, rosettes [42, 43] and concentric ring trajectories (CRT) [44–48][49] offering rapid coverage of the k -space, insensitivity to undersampling and motion artifacts and allowing ultra-short TE acquisition. Overall a scan time reduction up to 170-fold can be achieved. Therefore, k -space is sampled along trajectories (spatial information) while repeatedly measuring one single trajectory multiple times per TR (spectral information)[12]. However, due to the non-Cartesian sampling, the data points are not discretely gridded in k -space, hence, a more time-consuming reconstruction using re-gridding of data points or non-Cartesian discrete Fourier transform is required. [49].

Concentric ring trajectories (CRT), used in this thesis to measure tissue-specific relaxation times, are closed non-Cartesian trajectories. Each ring is measured multiple times per T_R using sine- and cosine-modulated in-plane gradients before increasing the radius of the circle for the next T_R , see figure 2.13. Due to their self-rewinding properties, CRT offers fast scanning times even for high spectral bandwidth and spatial resolution [50]. Scanning times of less than 3 min for a $32 \times 32 \times 31$ matrix were reported by Hingerl et al. [50].

Time-consuming relaxation time measurements could benefit from accelerated spatial-spectral encoding using CRT readout but require implementation of interleaved Inversion Recovery and Hahn Spin echo acquisition schemes, which is addressed in detail in section 3.1.

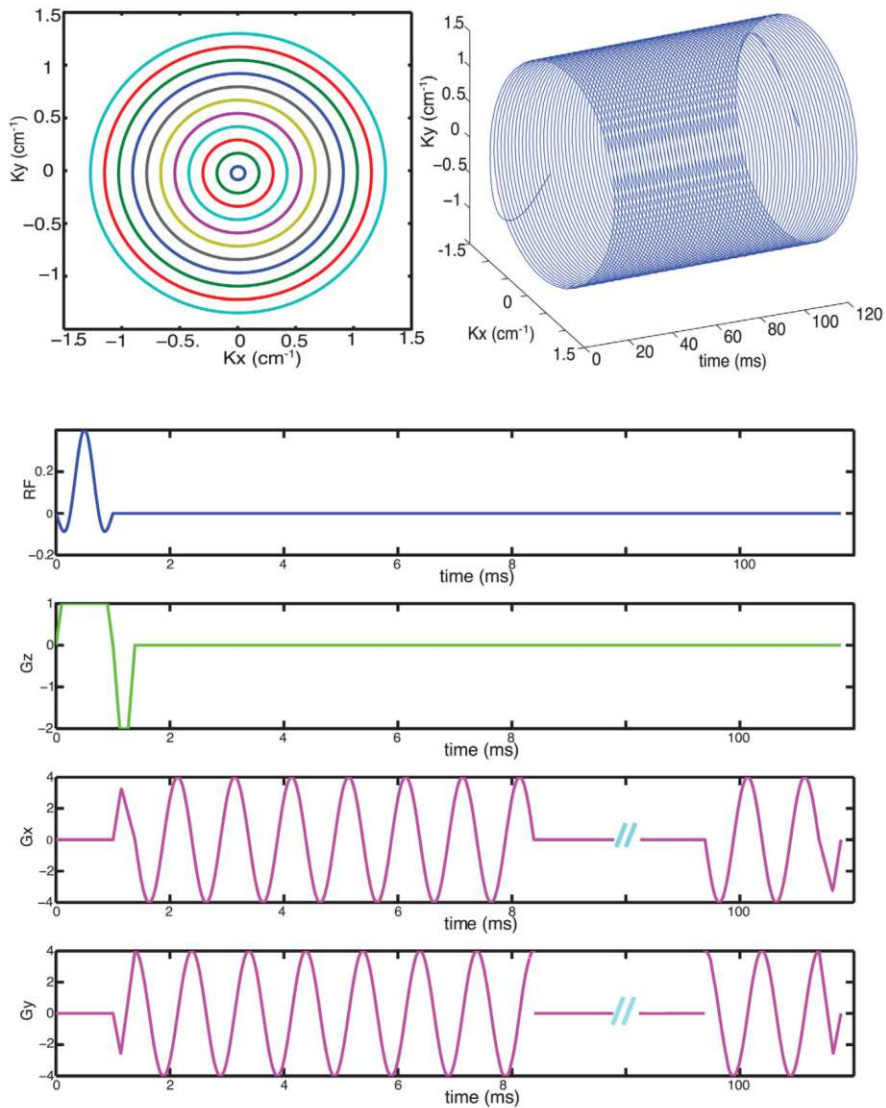


Figure 2.13: Schematic illustration of a CRT sequence: The upper left graph shows the concentric rings in k_x , k_y plane, which are sampled by sine- and cosine-modulated gradients. The frequency represents the angular velocity of the circle, which corresponds to the dwell time, and consecutively to the spectral bandwidth. The amplitude of the gradient corresponds to the radius of the circle. Each circle is measured multiple times per T_R before the gradient strength is increased and the next larger circle is sampled, see upper right graph. The bottom graph shows an illustration of a pulse sequence diagram. From the top to bottom: RF pulse, G_z , which is used to move along the z axis in k -space, and G_x , G_y , to move along the circular trajectories. Figure taken from [46].

2.5 Brain Metabolism

Glucose is the main energy source of the human brain, which is transported to the brain across the brain-blood barrier via cerebral blood flow (CBF) and metabolized to pyruvate in the cytosol during glycolysis. The majority of pyruvate (about 95%) is transported to the mitochondria where it is converted to Acetyl-CoA via pyruvate dehydrogenase (PHD), which is subsequently oxidized via the tricarboxylic acid (TCA) cycle [17, 25]. Excess pyruvate can also be converted anaerobically to lactate (Lac) via lactate dehydrogenase [26, 51]. The TCA cycle is a series of chemical reactions to generate energy in aerobic organisms in the form of adenosine triphosphate (ATP) in the mitochondria. Glutamate, an excitatory neurotransmitter, is converted from α -ketoglutarate in the TCA cycle. Furthermore, glutamate is converted to glutamine in the glutamate-glutamine cycle and serves as an immediate precursor of the inhibitory neurotransmitter gamma-Aminobutyric acid (GABA) [52]. Figure 2.14 provides an overview of glucose metabolism, illustrating how glucose is metabolized via glycolysis and oxygenic pathways in the downstream products glutamate and glutamine.

Impaired glucose metabolism is associated with numerous pathologies such as cancer, neurodegenerative diseases or diabetes [53–55]. In healthy tissue, glucose is metabolized oxidatively, whereas in tumor tissue glucose is anaerobically converted to lactate. This shift from healthy aerobic to anaerobic pathways is called the Warburg effect [55].

[^{18}F]-Fluorodeoxyglucose (FDG) positron emission tomography (PET) is the current clinical gold standard to detect cellular glucose uptake but requires invasive administration of radioactive tracers and does not give information about downstream metabolites due to glucose trapping in the cell. Deuterium metabolic imaging (DMI) is an emerging technique (MRS) to non-invasively map the cellular glucose uptake and downstream metabolism, presenting a promising alternative to FDG-PET. Both techniques will be discussed in the following subsections.

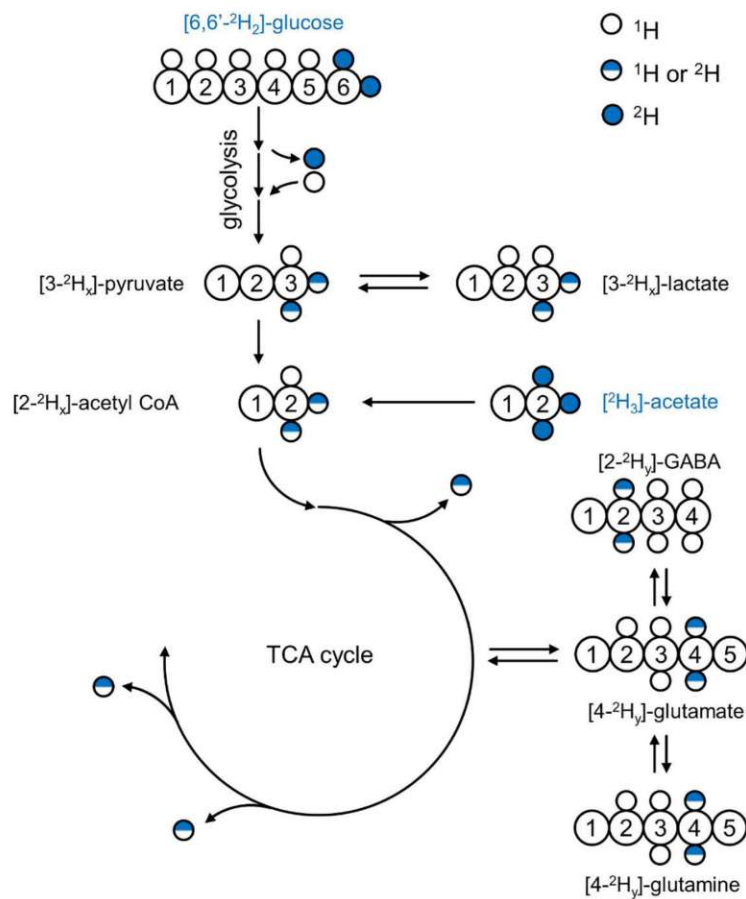


Figure 2.14: Schematic overview of the glucose metabolism in the human brain: Glucose is transported to the brain and metabolized via glycolytic and oxygenic pathways in the downstream products glutamate and glutamine. For numerous pathologies anaerobic pathways (Warburg effect) are enhanced leading to the production of lactate. Deuterated glucose is usually labeled on the C6 carbon position, illustrated in blue. After entering the TCA cycle deuterium is incorporated on the 4th carbon position of the downstream products glutamine and glutamate.

2.5.1 Positron Emission Tomography (PET)

Positron Emission Tomography (PET) is based on the simultaneous detection of two photons. Therefore, a positron-emitting radioactive tracer (i.e. Fluorodeoxyglucose ($[^{18}\text{F}]$ -FDG), is administered to the patient. Under β^+ -decay the nucleus emits a positron which after travelling a short distance (up to a few millimetres) annihilates with a nearby electron in the tissue. As a result, two photons are emitted in opposite directions, each with an energy of 511 keV due to the conversion of mass and energy. When two photons are detected within a coincidence time window (few ns) the origin of annihilation can be reconstructed [56, 57].

Fluorodeoxyglucose (FDG) positron emission tomography ($[^{18}\text{F}]$ -FDG PET) is the clinical gold standard for examining glucose uptake and metabolism. The positron-emitting isotope $[^{18}\text{F}]$ -FDG is metabolized similarly to glucose and can provide high-resolution contrast when tissue accumulates FDG in larger amounts as is the case in tumors [13, 22].

However, due to the reliance on the administration of unstable radioactive tracers, repetitive scanning to monitor disease progression is limited. Additionally, even though $[^{18}\text{F}]$ -FDG PET provides insight into glucose uptake, FDG is metabolically inert and cannot reveal the dynamics of downstream metabolic processes [16, 51]. Given the importance of these factors in diagnostics and treatment there is a growing demand for a non-radioactive and reliable approach to image glucose metabolism. Recently Deuterium Metabolic Imaging (DMI) has proven to be a suitable alternative to $[^{18}\text{F}]$ -FDG to non-invasively image the glucose metabolism.

2.5.2 Deuterium Metabolic Imaging (DMI)

While initial studies of ^2H NMR were already performed shortly after the invention of NMR [27, 58, 59] it took more than 40 years until deuterium was first used in vivo in 1986 by Brereton et al. [60] who studied the incorporation in triglycerides following the administration of heavy water in mice. And another 30 years until

recent publications by Lu et al. [26] and De Feyter et al. [16] evoke the interest of the scientific community [13].

Now, re-discovered, Deuterium metabolic imaging (DMI) is an emerging Magnetic Resonance Spectroscopic technique (MRS) to non-invasively map the cellular glucose uptake and downstream metabolism, using orally or intravenously administered deuterium-labeled glucose as safe and non-radioactive tracer [13, 16–18, 51, 61].

When non-ionizing deuterium-labeled glucose is administered as a tracer, it is taken up by brain cells and incorporated in the downstream products of glucose metabolism, i.e., glutamate and glutamine (Glx) and lactate (Lac). This allows a distinction between healthy oxidative and pathologic anaerobic pathways, which is not possible with [^{18}F]FDG-PET and thus represents one of the biggest advantages of DMI [7, 13, 14]. Typically, deuterated glucose labeled only the C1 and/or C6 carbon position is used for DMI. Labeling other carbon positions is not practical, as deuterium atoms would be lost to the water pool and not incorporated in the downstream products of interest (glutamine, glutamate or lactate). Glucose featuring deuterium atoms on more positions (C2-C5) is metabolized significantly slower compared to regular glucose. [13]. Throughout this thesis, deuterium-labeled glucose ([6,6']- ^2H -Glc) labeled at the 6th carbon position was used. During glucose metabolism deuterium is incorporated in the downstream products glutamine and glutamate at the 4th position, resulting in Glc₆ and Glx₄ (glutamine + glutamate) peaks in the ^2H MR spectra at 3.9 ppm and 2.4 ppm, respectively.

Deuterium is an isotope of hydrogen with a low gyromagnetic ratio and a Larmor frequency of 6.55 Mhz/T. The low natural abundance (0.015%) of deuterium results in sparse MRS spectra and less signal from interfering compounds such as water and lipids, compared to the conventionally used ^1H MRS where water and lipid signals are orders of magnitudes higher than the signals of the metabolites of interest. Since the deuterated water signal is small enough and in the range of the expected signal from labeled metabolites there is no need for water suppression in DMI and the water resonance can be used as an internal reference for concentration estimation [7, 13]. The sparsity of acquired DMI spectra allows for

simpler spectral quantification and, a 6.5-fold lower Larmor frequency makes DMI less sensitive to magnetic field inhomogeneities compared to ^1H MRS. Additionally, due to the low frequency of ^2H , which results in long wavelength, DMI is not affected by standing wave effects.

As discussed in section 2.2.1 for nuclei with spin quantum number $I \geq 1$, as is the case for deuterium $I = 1$, quadrupolar relaxation mechanisms are dominant, with only a minor contribution from dipolar relaxation with nearby protons and/or unpaired electrons. Given that dipolar relaxation scales proportionally with the square of the gyromagnetic ratio (see equations 2.10-2.12), the dipolar contribution to the relaxation of deuterium is only around 2.4% compared to hydrogen (proton). The dominance of the quadrupolar moment of deuterium leads to relatively short spin-lattice (T_1) and spin-spin (T_2) relaxation times, which allows for shorter repetition times (T_R) leading to overall lower scan times than conventional ^1H acquisitions. Generally, T_1 and T_2 relaxation constants of ^2H are relatively independent of the magnetic field strength. While it is expected that T_1 relaxation shows a slight increase with the magnetic field strength, T_2 relaxation times tend to decrease slightly with the magnetic field strength [13]. T_1 relaxation times of 50-60 ms, 150-200 ms and 350 ms and were reported for Glc, Glx and water, in the human brain, respectively. Additionally, T_2 relaxation times of 20-30 ms for water and below 50-60 ms for metabolites were reported for the human brain [13, 16].

DMI represents a simple, non-invasive, and robust MR-based method to map the glucose uptake and downstream metabolism with high temporal and spatial resolution and is a promising alternative to FDG-PET which relies on the administration of a radioactive tracer and does not give information about downstream metabolites due to glucose trapping in the cell.

3 Materials and Methods

3.1 Implementation of Inversion Recovery and Hahn Spin-Echo into CRT sequence

A 3D FID-MRSI sequence using non-cartesian CRT readout was extended, to allow spatially resolved assessments of relaxation time constants (T_1/T_2). The novel sequence was then applied in the human brain to assess tissue-specific relaxation times of deuterium labeled metabolites, i.e., glucose and combined glutamate+glutamine (Glc, Glx) in WM and GM dominated regions.

For sequence programming, Siemens provides a programming environment called IDEA (Integrated Development Environment for Application), based on the programming language C++, hence, sequence code is structured in header files for object and variable declaration i.e. RF pulses, gradients and ADCs (Analog-digital converters) (e.g., *example.h*) and .cpp files for definitions of object and functions *example.cpp*. Generally, all sequences consist of five main functions: Initialize(), Prepare(), Check(), Run(), RunKernel(). All sequence parameters including the user interface visible on the simulator or the scanner, are once initialized in the Initialize() function. Sequence simulation and debugging can be performed using the Protocol offline editing tool (POET) simulating the user interface of a real scanner. Measurement parameters can be adjusted individually, to fully simulate a measurement and sequence structure is visualized as RF-pulses, gradients, and ADCs on a time graph. The Prepare() function monitors and validates each parameter adjustment, repeatedly running in the background while the user adapts

the settings. Before the actual scanning, the `Check()` function verifies once if all settings are correct. In the `RunKernel()` function, the actual sequence timing is defined for each RF pulse, gradient, or ADC. The `RunKernel()` usually represents a single repetition (TR), which is called multiple times (depending on the number of averages, repetitions, or prescans that have been set) within the `Run()` function, which is executed only once. Individual input fields and selection boxes can be freely implemented on a user-defined special card within the standard user interface of the MR scanner.

In the course of this thesis, an already existing 3D ^2H -FID-MRSI sequence using CRT readout [19] was modified by implementing Inversion recovery (180° pulse - 90° pulse) and Hahn spin-echo (90° pulse - 180° pulse) acquisitions schemes. The original sequence used 3D density weighted sampling of the k -space, which acquires the k -space in a Hamming-weighted fashion, i.e., the k -space center is weighted stronger than the periphery. Inversion Recovery and Hahn Spin-Echo acquisitions were implemented in an interleaved manner, i.e., each trajectory was repeatedly acquired with variable inversion or echo times before increasing the radius for the next circle trajectory, see figure 3.1. The main advantage of this approach is, that relaxation time assessments become relatively independent from variations in metabolite concentration, which can not be ruled out in an experiment using tracer agents, such as deuterium labeled glucose, even though a steady-state can be assumed within a certain time frame. Additionally, sampling of the 3D k -space was performed "inside out" (starting in the center and moving outwards) acquiring high signal amplitudes in the beginning of the measurement, which minimizes potential effects of decreasing metabolite concentrations in later parts of the measurement. To compensate for unwanted excitation due to imperfect RF pulses, spoiler gradients in xyz -direction were inserted, symmetrically, before and after for 180° -refocusing or after 180° inversion for T_2 and T_1 measurements, respectively.

A drop-down menu was created on the special card to switch between different measurement modes: normal or T_1 and T_2 relaxation time measurements. The number of inversion or echo times can be individually modified by inserting nu-

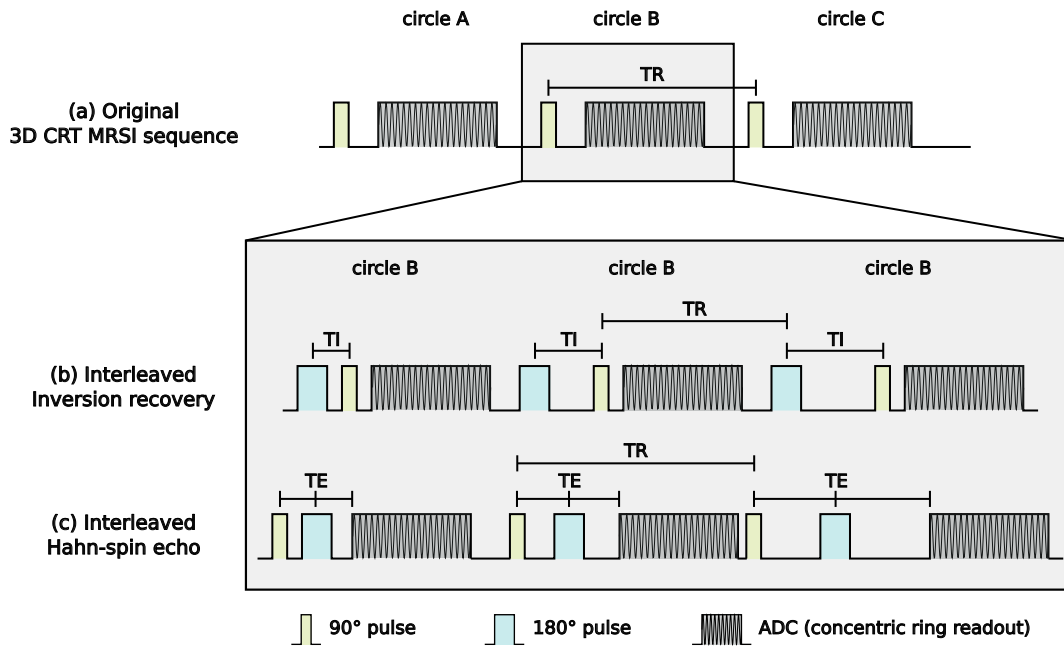
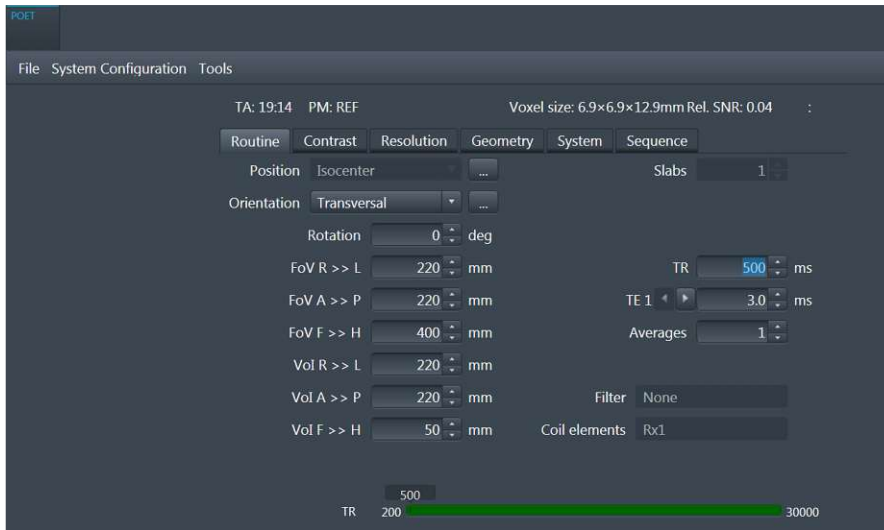


Figure 3.1: Simplified illustration of the original 3D FID ^2H -MRSI sequence with three representative concentric ring trajectories A-C (a). Inversion recovery (b) and Hahn spin-echo (c) acquisition schemes were implemented in an interleaved manner. Each ring trajectory is measured consecutively with variable inversion and echo times while k -space is sampled from k -space center outwards.

meric values given in ms. Additionally, unlocalized FID acquisitions were temporally interleaved (after a defined number of repetition times TR) to monitor global Glc and Glx levels throughout the measurement, which could be used for retrospective correction of unexpected strong fluctuations of metabolite concentrations. This feature can be activated by ticking a box on the special card. The operator can freely choose between equidistant and hamming weighted k -space sampling and whether the k -space should be measured from the k -space center outwards or from top to bottom, see screenshot of the special card shown in figure 3.2b. Additionally, in case of density weighted k -space sampling, the number of acquired circles can be increased, which has in principle the same effect as signal averaging, effectively increasing acquisition duration.



(a) POET



(b) Special Card

Figure 3.2: POET can be used to simulate a measurement like on a real scanner (a). On the special card, individual parameters can be stored and adjusted by the operator during the measurement. The operator can choose between a normal measurement and T_1 and T_2 measurements via a drop-down menu. The number of inversion/echo times can be set and the numeric values can be typed in. Additionally, it is possible to activate unlocalized FID acquisitions every i.e. 70th TR to monitor Glc and Glx levels.

3.2 MR scanner

The core component of every MR scanner is its strong homogenous magnetic field. Nearly all modern MR scanners utilize superconduction magnets, featuring zero electrical resistance below a material characteristic critical temperature T_C (roughly below 9.4 K) and expulsion of internal magnetic fields (Meissner effect) but require cooling with liquid helium. Commonly niobium-titanium (NbTi) alloys are embedded in a copper matrix and wound in a solenoidal fashion around the scanner tube. As long as the filaments are cooled below T_C , electrical current can flow continuously without energy loss creating a strong magnetic field up to several T.

Besides the superconducting magnet, the scanner also possesses shim coils to further improve the homogeneity of the magnetic field B_0 , a gradient coil system for spatial encoding and radiofrequency coils for transmission and reception of the NMR signal [7]. The latter are discussed in more detail in the next chapter.

The only 7T MR scanner (Terra-dot-Plus, Siemens Healthineers, Erlangen Germany) in Austria is located at the Highfield MR Center, of the Medical University of Vienna (see figure 3.3), with a gradient system featuring a maximum amplitude of 70 mT/m with a nominal slew rate of 200 T/m/s.



Figure 3.3: Experimental 7T whole-body MR scanner from Siemens, located at the Highfield MR Center. Figure taken from [62].

3.3 Radiofrequency coil

For signal transmission and reception radiofrequency (RF) coils are used which can generate short RF pulses to excite the magnetization into the transverse plane and simultaneously function as a receiver for signal detection. Due to shortened wavelengths in the range of the measured object as a result of higher Larmor frequencies (for ^1H), 7T MR scanners are not equipped with a built-in RF body coil system. Therefore, external RF coils have to be used for signal transmission and reception. Depending on the measurement, different commercially available and in-house built coils are available. For relaxation time experiments conducted during this thesis, a dual-tuned quadrature bird-cage volume coil (Stark Contrast MRI Coils Research, Germany) (see figure 3.4) was used, which allows to detect both ^1H and ^2H signals with the same coil.

Although multi-channel surface coil arrays offer improved signal-to-noise ratio (SNR), signal reconstruction, including coil combination and weighting, becomes more complex. In contrast, volume coils offer a more homogeneous magnetic field



Figure 3.4: $^2\text{H}/^1\text{H}$ dual-tuned quadrature bird-cage head coil used for phantom and in vivo relaxation time experiments.

B_1 , ensuring uniform excitation throughout the sample, which is particularly important for relaxation time experiments.

3.4 Deuterium Labeled Glucose

Deuteration of molecules is a simple chemical procedure, replacing hydrogen atoms in a specific molecule by deuterium atoms. This can be performed, in principle, for any given molecule, which allows for labeling broad ranges of different substances. During the course of this work deuterium labeled $[6,6']\text{-}^2\text{H}$ glucose was used, featuring deuterium atoms on the 6th carbon position. As conventional glucose, $[6,6']\text{-}^2\text{H}$ Glc is transported via the blood stream and absorbed by the brain cells. During oxidative glucose metabolism, deuterium is incorporated on the 4th carbon position of the downstream products glutamine and glutamate, resulting in Glc_6 and Glx_4 (glutamine + glutamate) peaks in the ^2H MR spectra at 3.9 ppm and 2.4 ppm, respectively.

Deuterated glucose (Cambridge Isotopes) was purchased in powder form with a purity of >99% and dissolved in 200 ml water using 0.8 g/kg body weight before oral administration during in vivo relaxation time experiments.

3.5 Measurement Protocol

All measurements were performed on an experimental 7T (Terra-dot-Plus) Siemens whole-body MR system using a $^2\text{H}/^1\text{H}$ dual-tuned quadrature bird-cage head coil (Stark Contrast MRI).

The modified 3D ^2H -FID-MRSI sequence with CRT readout for relaxation time measurements was validated on a spectroscopic water phantom (glass sphere with a diameter of 160 mm containing water with added lithium lactate: 96 mM and sodium acetate: 100 mM) from Siemens to detect natural abundance water and results were compared with values obtained by a non-localized FID sequence, which was chosen as a reference gold standard. The following parameters were applied: voxel volume = 1.96 ml, matrix size = 16 x 16 x 15, $TR = 1500$ ms; $TE = 2$ ms; six TIs : 5 - 1500 ms; seven TEs : 10 - 1000 ms.

Eight healthy volunteers (7m/1f) without a history of neurological, psychiatric, or metabolic diseases were scanned after written informed consent was obtained. Scans were performed in the morning after overnight fasting and 90 min after oral $[6,6']\text{-}^2\text{H}$ glucose administration (0.8 g/kg body weight) during steady state, see figure 3.5.

The study protocol included an automated alignment localizer to localize the position of the water phantom and the brain of the volunteer followed by B_0 shimming using the standard shimming routine supplied by Siemens and manual shimming to reduce B_0 inhomogeneities. To find the optimal reference voltage to approximate 90° excitation and 180° inversion/refocusing flip angles, unlocalized pulse-acquire B_1 mapping was applied. In vivo scans included anatomical MP2RAGE acquisitions which were later used for WM and GM tissue segmentation followed by the

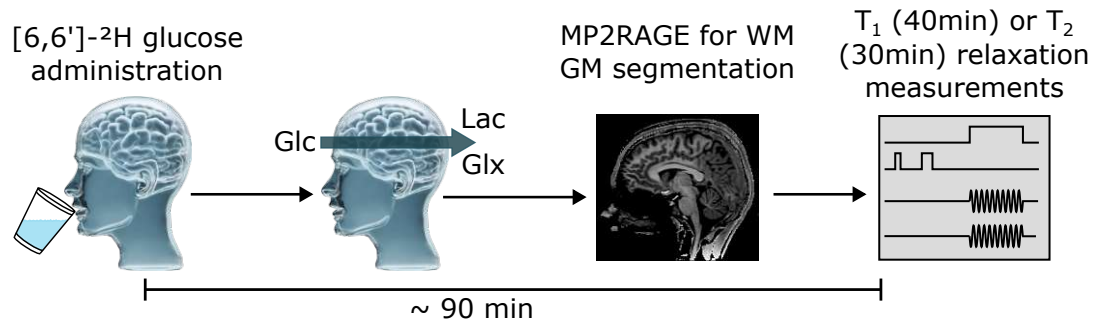


Figure 3.5: Illustration of the in vivo measurement protocol: Relaxation measurements were performed approximately 90min after oral glucose administration following MP2RAGE acquisitions for WM and GM segmentation.

actual MRSI measurements. The 3D-MRSI (either T_1 or T_2) protocol was employed 90 min after glucose intake using the following parameters: FOV = 200 x 200 x 192 mm; matrix size = 22 x 22 x 21; nominal isotropic volume = 0.75 ml; 148 samples; TR_{T_1/T_2} = 500/400 ms; six TIs : 5 - 500 ms; eight TEs : 6 - 60 ms, TA_{T_1/T_2} = 40/30 min. Additionally, one subject was remeasured without glucose administration to measure relaxation times of natural abundance water (TR_{T_1/T_2} = 900/400 ms; five TIs : 5 - 900 ms; six TEs : 6 - 60 ms).

3.6 Data Reconstruction

Data was reconstructed using in-house developed post-processing pipelines (MATLAB R2021, LCModel v6.3, Python v3.10), including non-cartesian three-dimensional discrete Fourier Transformation. High-resolution MP2RAGE images were segmented using FAST [63] and downsampled to match the spatial resolution of the MRSI data, while considering effects of the point spread function and partial volume contamination of the increased voxel volumes. Additionally, to further decrease partial volume contamination effects only WM or GM voxels featuring more than 60% tissue fraction were included in the analysis. Partial volume effects

occur when a single voxel contains different types of tissue in our case WM, GM or CSF.

Due to inherently low signal-to-noise ratios per voxel (SNR)/voxel, it was not possible to map the relaxation time constants over the whole brain. Thus, spectral data was averaged separately for GM and WM regions, before spectral fitting.

3.7 Spectral Fitting

Spectral fitting was performed voxelwise for phantom and over regionally averaged data for in vivo measurements in the frequency domain using LCModel [64]. LCModel is a linear combination model that tries to fit a given basis set of spectral components to the measured frequency spectrum using linear combination and minimizing iteratively the residuum.

Basis sets were simulated with different acquisition delays (T_1 : 2 ms, T_2 : 0 ms) using jMRUI [65, 66] to match the first-order phase of the acquired data. The peaks were of Lorentzian shape and following simulation a 10 Hz line broadening was applied. For phantom measurements, a basis set featuring only a water peak at 4.8 ppm for the natural abundance water was used. In vivo, a custom-built basis set was created for spectral fitting featuring ^2H resonances of water (4.8 ppm), Glc (3.9 ppm), and Glx (2.4 ppm) and unconventionally included corresponding metabolite peaks with 180° phase offset, which were required due to significantly different T_1 relaxation time constants between water, Glc, and Glx. LCModel does not correct phase offsets individually for each metabolite, and by using a regular basis set without phase offset would decrease the fitting accuracy and would lead to inferior results. A script (bash, Matlab R2023) was written including prior knowledge to individually select between metabolic peaks with inverted or regular phase depending on the TI and estimated relaxation time of the metabolites.

3.8 Data Evaluation and Statistical Analysis

Exponential fitting of the relaxation time constants was done assuming a 3 variable fit for T_1 relaxation:

$$M(TI) = C_1(1 - C_2 * e^{-TI/T_1}) \quad (3.1)$$

and a 2 variable fit for T_2 relaxation:

$$M(TE) = C_1 * e^{-TE/T_2}. \quad (3.2)$$

For exponential fitting of unlocalized FID acquisitions, a bi-exponential fit was used, to account for different compartments in the human brain. In alignment with [16, 18] longer relaxation times were assumed for extracellular fluid (CSF) (18.5%) and shorter relaxation times for intracellular fluid (82.5%):

$$M_{\text{bi-exp}}(T_E) = C_1 * 17.5 e^{-TE/T_2^{\text{long}}} + C_2 * 82.5 e^{-TE/T_2^{\text{short}}}. \quad (3.3)$$

Paired t -test was used to test for significant differences between GM, WM, and non-localized FID relaxation time constants. A statistical significance threshold of $p < 0.05$ was applied. Relaxation time analysis and statistical tests were performed using Python (v3.10, `curve_fit` function from `scipy.optimize` and `scipy.stats`).

Glc and Glx levels were additionally monitored during in vivo measurements. The spectra resulting from the individual non-localized FIDs over time were analyzed using jMRUI and spectral fitting was performed in the time domain using the AMARES (Advanced Method Accurate Robust and Efficient Spectral Fitting) algorithm [67]. To analyze temporal stability of metabolite concentrations, coefficients of variation (COV) were calculated throughout the whole experiment for all volunteers according to:

$$\text{COV} = \rho/\mu, \quad (3.4)$$

with ρ representing the standard deviation and μ the arithmetic mean. A lower CV indicates more stable Glc/Glx levels.

4 Results

After the CRT-based 3D MRSI sequence was modified allowing spatially resolved relaxation time mapping. The sequence was tested on a phantom to validate that Inversion Recovery and Hahn spin-echo acquisition schemes were correctly implemented. Therefore, derived T_1 and T_2 relaxation time constants from data acquired using the CRT sequence were compared to the defined reference gold standard data obtained with an unlocalized FID sequence. Afterwards, the sequence was tested in vivo, to determine relaxation time constants of deuterium labeled glucose and combined glutamate+glutamine (Glx), 90 min after oral administration of deuterium labeled glucose.

4.1 Phantom

Signal to noise ratio was sufficiently high to create relaxation time maps from data acquired using the CRT sequence, i.e., T_1 and T_2 values were calculated voxelwise and additionally, to compare it with unlocalized FID acquisitions, from averaged spectra of the entire volume of the phantom. Calculated T_1 and T_2 relaxation times were consistent between CRT-based 3D-MRSI and non-localized FID acquisitions. Representative fits of T_1 and T_2 relaxation constants of the 3D CRT-based and FID sequence are shown in figure 4.2 and measurement values are listed in table 4.1.

	CRT _{voxelwise}	CRT _{averaged}	FID
T_1 [ms] :	424 ± 43	423 ± 3	428 ± 3
T_2 [ms] :	471 ± 28	421 ± 11	442 ± 4

Table 4.1: T_1 and T_2 Relaxation time constants obtained with CRT-based 3D-MRSI and non-localized FID acquisitions in a water phantom are in good agreement.

Since the phantom contains mostly water, relaxation effects are homogenous across the entire volume. Therefore derived T_1 and T_2 relaxation times acquired spatially localized using CRT and unlocalized FID values were expected to be equal. While the longitudinal relaxation time constants were in the range of around 423 ms, deviations were observed for transversal relaxation constants (CRT_{voxelwise} vs FID: +11%, CRT_{averaged} vs FID: -5%). This can presumably be explained, as reliable fitting of an exponential decay (Hahn spin-echo) is more prone to fitting errors compared to an exponential increasing function (Inversion recovery). For the latter, there are high SNR values for short and long inversion times, which allows for more reliable spectral fitting, yielding more robust results. Conversely, the SNR during Hahn-spin echo experiments decreases with increasing echo times, posing challenges for spectral fitting, particularly for longer echo times. Although signal weighting of high SNR measurement points was tested during data analysis, it did not increase fitting accuracy. However, derived relaxation times between CRT and unlocalized FID acquisitions were in close approximation.

Additionally, relaxation time maps of T_1 and T_2 constants (voxelwise analysis), depicted in figure 4.1, show that both maps appear homogenous featuring only few outliers, which indicates similar relaxation times between voxels, which was anticipated. This is quantitatively reflected by low coefficients of variation (COV) of 10% and 6% for T_1 and T_2 relaxation times, respectively.

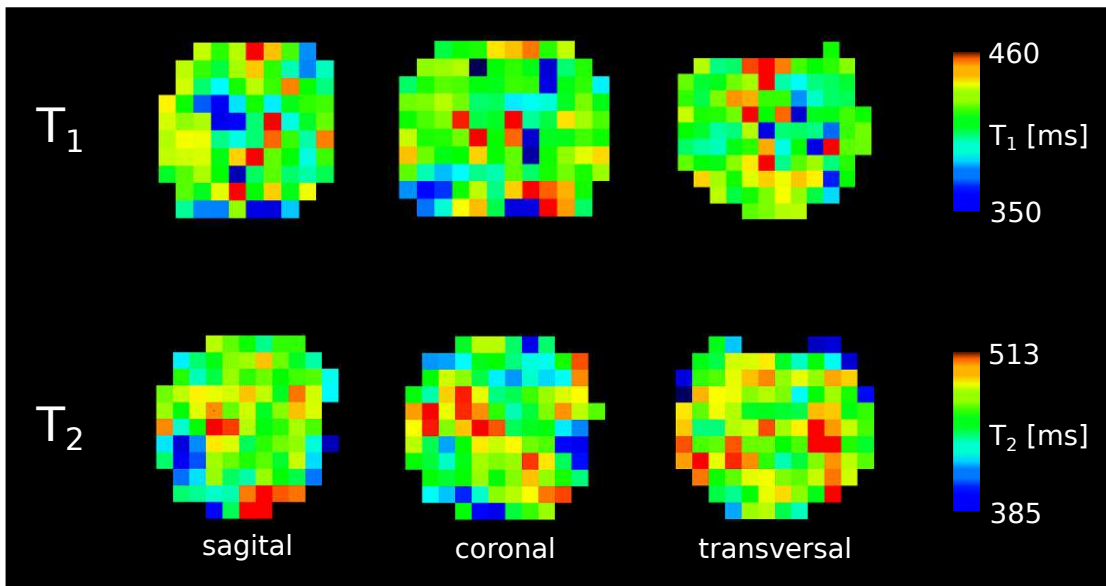


Figure 4.1: Relaxation time maps of the water phantom for T_1 (top) and T_2 (bottom) relaxation time experiments. Both maps appear homogenous and only a few outliers are visible.

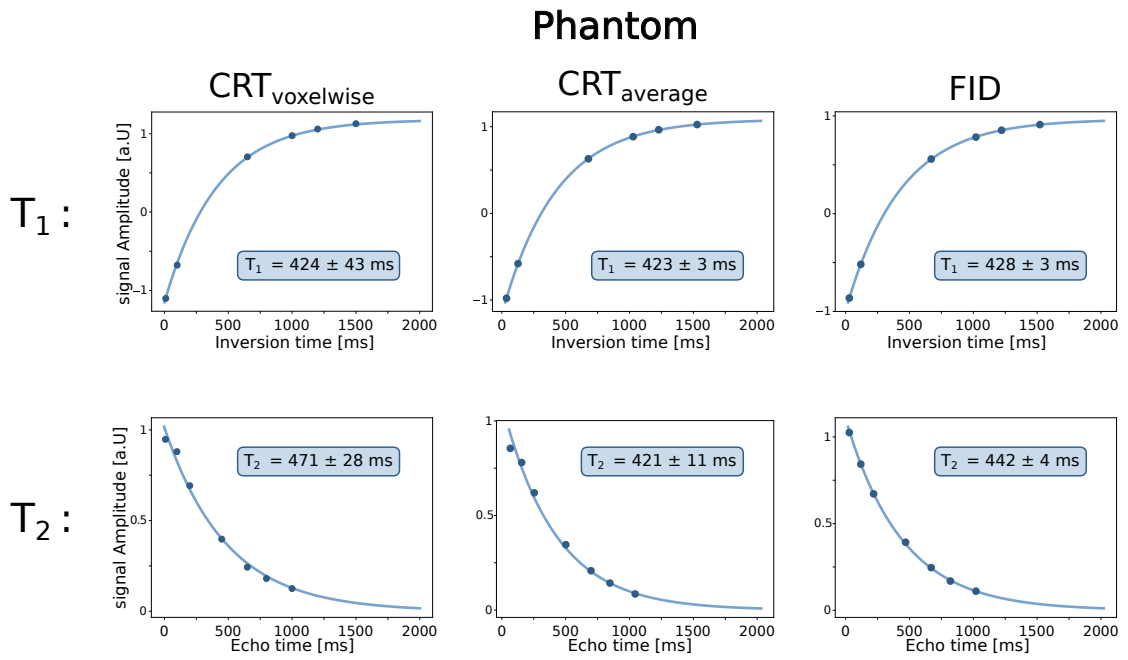


Figure 4.2: Representative exponential fits to quantify the T_1 and T_2 relaxation times of natural abundance water in the phantom in vitro. A newly developed 3D MRSI sequence using concentric ring trajectory readout was validated by comparing relaxation time constants to values obtained by an unlocalized FID sequence.

4.2 In vivo

Tissue-specific T_1 and T_2 relaxation times of the downstream products Glc and combined glutamate+glutamine (Glx) were determined after oral administration of deuterated glucose. Relaxation time constants of the natural abundance water of one volunteer were additionally obtained.

4.2.1 Natural abundance Water

In vivo, T_1 and T_2 values of the natural abundance water were measured in one volunteer without glucose administration. Tissue-specific T_1 and T_2 relaxation constants of gray and white matter dominated regions of the human brain acquired using the 3D CRT-based MRSI sequence were comparable with results obtained with non-localized FID scans. Values are listed in table 4.2 and exponential fits of relaxation time constants are shown in figure 4.3. For exponential fitting of the unlocalized FID acquisitions, a bi-exponential fit was used, considering that in the brain there are different compartments with substantially different relaxation mechanics (extracellular fluid: cerebral spine fluid (CSF) and intracellular fluid: GM, WM).

In agreement with literature, shorter longitudinal relaxation times were measured in WM than in GM but only one volunteer was measured. Hence, no reliable statistical prediction can be made whether relaxation times of the natural abundance water are significantly different in WM or GM before investigating a higher number of volunteers. Additionally, faster transversal relaxation, i.e., shorter T_2 constants were acquired in WM dominated regions compared to GM. To the best of our knowledge, the acquisition of tissue-specific transversal relaxation times has not been performed previously. The comparison of results between CRT- and FID-based acquisition schemes, should serve only as an approximation and could identify strong systematic measurement errors, even if relaxation time constants vary across different tissue types.

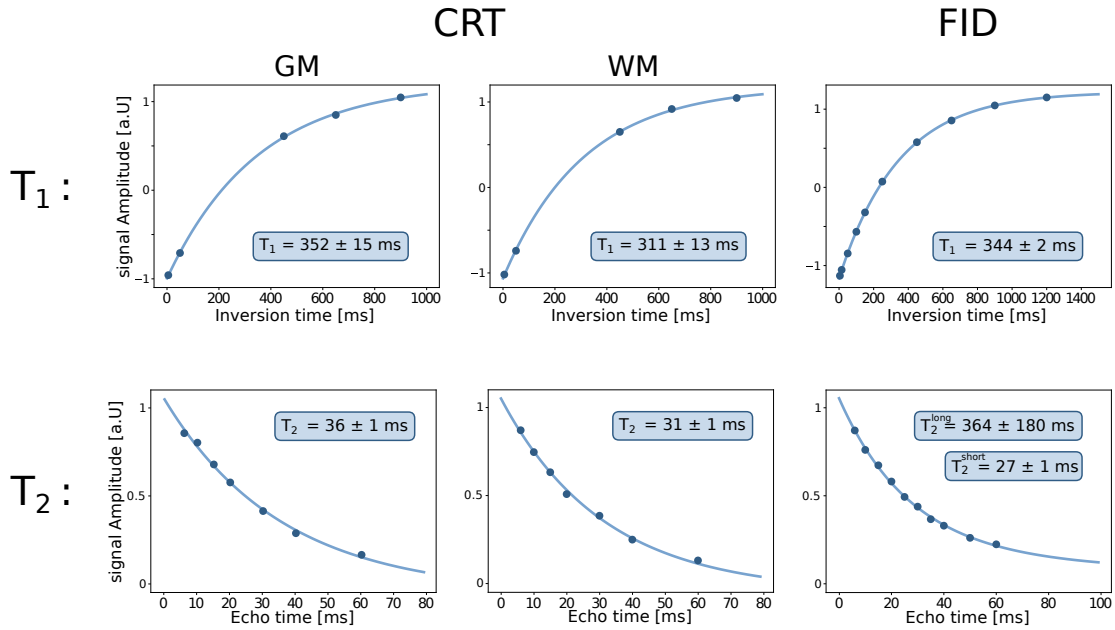


Figure 4.3: Representative exponential fits from one healthy volunteer to quantify T_1 and T_2 relaxation times constants of the natural abundance water. Scans were performed without glucose administration and data was acquired using a 3D MRSI sequence using concentric ring trajectory readout, which enabled measuring relaxation times separately in gray and white matter and compared to an unlocalized FID. FID T_2 relaxation constants of water were fitted using a bi-exponential fit.

	CRT _{GM}	CRT _{WM}	FID
T_1 [ms] :	352 ± 15	311 ± 13	344 ± 2
T_2 [ms] :	36 ± 1	31 ± 1	short: 27 ± 1 long: 364 ± 180

Table 4.2: Relaxation time constants of the natural abundance water obtained with CRT-based 3D-MRSI and non-localized FID acquisitions in vivo. Values obtained with the new CRT sequence are in the same range as values obtained with the unlocalized FID sequence. Scans were performed without glucose administration. Taking into account longer T_2 relaxation times for CSF, transversal relaxation constants of water were fitted using a bi-exponential fit for unlocalized FID acquisitions.

4.2.2 Orally administered deuterated Glucose

Tissue-specific relaxation time constants of the downstream products Glc and Glx were determined in the presumed steady-state phase approximately 90 min after oral administration of deuterated glucose.

Shorter T_1 relaxation times were measured for Glc: $T_1^{\text{GM/WM}} = 56 \pm 14/60 \pm 19$ ms compared to Glx: $T_1^{\text{GM/GM}} = 167 \pm 22/173 \pm 12$ ms. T_2 relaxation times for both metabolites were in a similar range of 30-40 ms (Glc: $T_2^{\text{GM/WM}} = 37 \pm 1/36 \pm 2$ ms; Glx: $T_2^{\text{GM/WM}} = 36 \pm 1/34 \pm 2$ ms). Tissue-specific relaxation time constants acquired using the 3D CRT-MRSI sequence are in good agreement with unlocalized T_1 and T_2 times presented in recent literature[16–18]. Individual results are listed in table 4.3 and representative exponential fits of T_1 and T_2 relaxation constants are shown in figure 4.5 and 4.6, respectively.

Relaxation times were not significantly different between GM- and WM dominated regions for Glc (T_1 : $p = 0.37$; T_2 : $p = 0.42$) and Glx (T_1 : $p = 0.58$; T_2 : $p = 0.13$). Differences between CRT and FID acquisitions could be observed for GM (T_1 : $p_{\text{Glc}} = 0.001$; T_2 : $p_{\text{Glx}} = 0.02$) and WM (T_1 : $p_{\text{Glc}} = 0.03$; T_2 : $p_{\text{Glx}} = 0.02$).

Representative averaged sample spectra for increasing TI and TE times during T_1 (Inversion-Recovery) and T_2 (Hahn-Spin-Echo) acquisition schemes are illustrated for one representative volunteer, see figure 4.4 a,d. Additionally, high-SNR averaged sample spectra from the first inversion/echo time acquired with the CRT-based and unlocalized FID sequence are highlighted in more detail, see figure 4.4 b,c,e,f.

Approximately 90 min after glucose administration it is assumed that Glc and Glx levels are in a relatively steady state phase for another 60-80 min. To monitor the stability of Glc and Glx levels throughout the measurement protocol unlocalized FID acquisitions were measured every 70th TR (i.e., roughly every 35 seconds). Evaluation of the dynamic FID data revealed relatively stable Glc and Glx levels throughout the measurements with a coefficient of variation of $6\pm 1\%$ and $7\pm 1\%$, respectively.

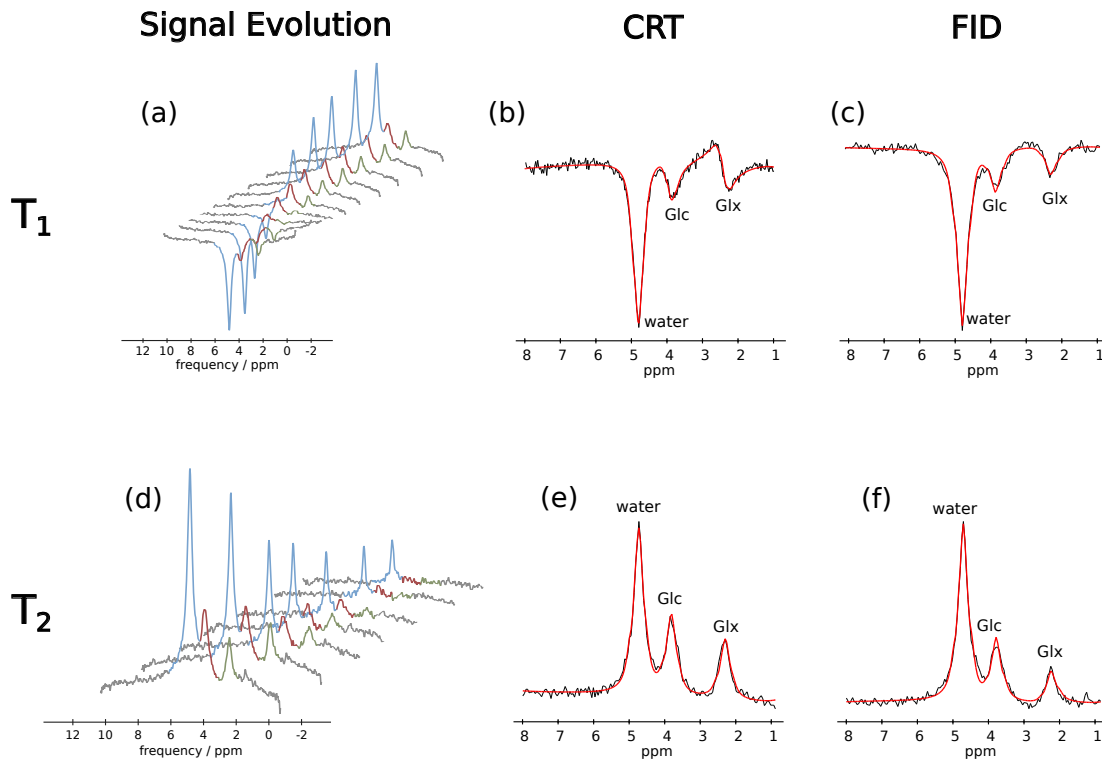


Figure 4.4: Series of spectra acquired during T_1 (a) and T_2 (d) measurements with the FID sequence illustrating the signal evolution for increasing TI/TE . The relaxation dynamics are clearly observable with Glc (red peak) featuring the shortest relaxation time constant and the fastest relaxation followed by Glx (green peak) and water (blue peak). Sample spectra (black) and corresponding spectral fit (red curve) of the first TI/TE acquired using CRT-based MRSI (spectra from GM region) and unlocalized FID sequence in one representative volunteer for inversion Recovery (b,e) and Hahn spin-echo (c,f) experiments, featuring resonances of the natural abundance water, Glc and Glx.

Subject	Glc			Glx			
	FID	CRT		FID	CRT		
		GM	WM		GM	WM	
T_1 [ms]	1	55 ± 6	38 ± 10	41 ± 10	140 ± 12	162 ± 35	166 ± 45
	2	57 ± 7	48 ± 4	39 ± 8	154 ± 15	138 ± 24	170 ± 40
	3	66 ± 7	56 ± 7	63 ± 9	179 ± 20	183 ± 30	158 ± 33
	4	57 ± 5	74 ± 8	83 ± 5	158 ± 9	192 ± 25	179 ± 25
	5	82 ± 3	66 ± 4	72 ± 8	163 ± 8	184 ± 12	158 ± 14
Mean ± SD	69 ± 15	56 ± 14	60 ± 19	159 ± 14	167 ± 22	173 ± 12	
T_2 [ms]	6	32 ± 1	36 ± 1	34 ± 1	31 ± 2	36 ± 1	33 ± 3
	7	35 ± 2	37 ± 1	38 ± 1	32 ± 1	35 ± 3	34 ± 4
	8	33 ± 2	38 ± 1	36 ± 2	31 ± 3	36 ± 2	35 ± 3
	Mean ± SD	33 ± 2	37 ± 1	36 ± 2	31 ± 1	36 ± 1	34 ± 1

Table 4.3: In vivo T_1 (top) and T_2 (bottom) relaxation times [ms] for deuterated resonances Glc and Glx in the human brain were measured in eight healthy volunteers after oral administration of $[6,6']\text{-}^2\text{H}$ glucose. Relaxation times are given for non-localized FID scans and localized to gray and white matter using 3D CRT-MRSI. No significant differences were found between GM and WM dominated regions, while differences between FID and CRT acquisitions were observed.

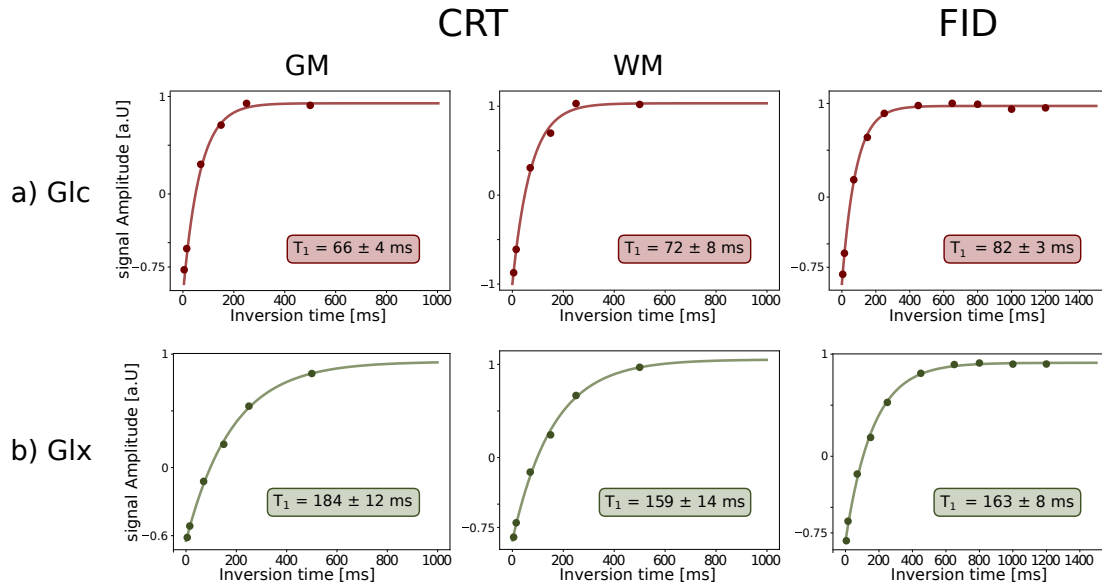


Figure 4.5: Representative exponential fits for Inversion recovery experiments to quantify the T_1 relaxation constants of glucose (red) and combined glutamate+glutamine (Glx) (green) from one healthy volunteer after oral administration of deuterated glucose. Data were acquired using a 3D MRSI sequence using concentric ring trajectory readout, which enabled measuring relaxation times separately in gray (GM) and white matter (WM) and compared to an unlocalized FID.

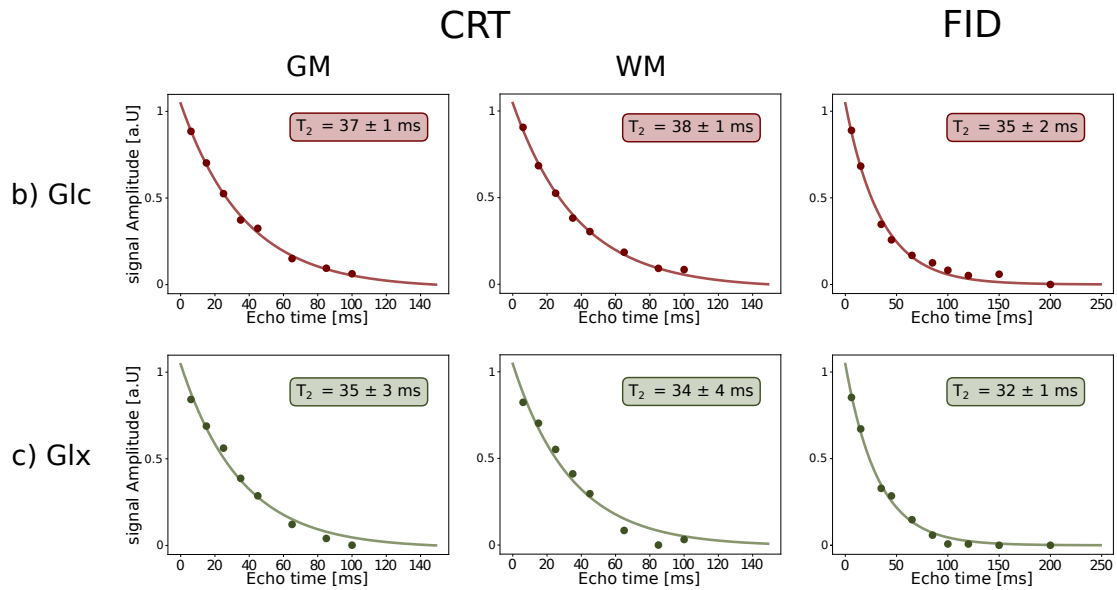


Figure 4.6: Representative exponential fits for Hahn spin-echo experiments to quantify the T_2 relaxation constants of glucose (red) and combined glutamate+glutamine (green) from one healthy volunteer after oral administration of deuterated glucose. Data were acquired using a 3D MRSI sequence using concentric ring trajectory readout, which enabled measuring relaxation times separately in gray and white matter and compared to an unlocalized acquisition method.

5 Discussion

In the course of this thesis, a 3D ^2H -FID-MRSI sequence using Hamming-weighted non-Cartesian concentric ring trajectory (CRT) sampling was successfully modified to measure tissue-specific T_1 and T_2 relaxation times of deuterium resonances (water, glucose, glutamine+glutamate) in the human brain.

The developed 3D MRSI-based sequence was first validated on a water phantom. Consistent results were obtained and compared to data acquired using unlocalized FID acquisitions (defined gold standard). Sufficiently high signal-to-noise ratios allowed for voxelwise analysis and relaxation time mapping of the water phantom. Homogenous relaxation time values were observed throughout the entire volume featuring a low coefficient of variation ($\text{COV} < 10\%$). Observed T_1 and T_2 relaxation times of the natural abundance water in phantom were in good agreement with results reported in [18] although De Feyter et al. [16] reported shorter T_2 values of around 372 ms. This could be presumably explained as the phantom used during the course of this work, does not solely contains water, but also lithium lactate and sodium acetate, which could alter T_2 relaxation values.

Due to limited signal-to-noise ratios achieved for in vivo experiments, voxelwise mapping of relaxation times was not feasible, and spectral averaging was performed to increase the SNR substantially. Regional averaging over WM and GM dominated regions, allowed for reliable spectral fitting and tissue-specific relaxation time determination of ^2H glucose and ^2H glutamate+glutamine, which to the best of our knowledge has not been done before except for natural abundance water.

In vivo relaxation times of the natural abundance water were obtained from one healthy volunteer and results were in the same range as reported T_1 values for GM and WM reported by Cocking et al. [15] and unlocalized T_1 and T_2 values [13, 16, 18]. Based on a single volunteer measurement, no statement can yet be made regarding a significant difference between GM and WM regions and more volunteers have to be measured in the future, but considering the amount of effort for multiple time consuming measurements and the lack of novelty, this exceeds the scope of this thesis.

Tissue-specific relaxation times of deuterium resonances Glc and Glx were determined after orally administering deuterated glucose. To accurately measure relaxation constants, measurements were performed in the steady state where Glc and Glx levels are assumed to be constant. Glc and Glx levels were therefore monitored during the measurement and showed low coefficients of variation ($COV < 7\%$). Observed relaxation times of Glc and Glx for GM and WM dominated regions are in good agreement with unlocalized values measured in this thesis and reported in literature [13, 16, 18], yet no differences were found between GM and WM values. While tissue-specific T_1 values of Glc are in the same range compared to unlocalized values, determined values for Glx are higher, but values are within the standard deviation. De Feyter et al. [16] reported T_2 values of Glc and Glx in the human brain at 4T and lower values at 11.7T in rat brain. T_2 relaxation times in this work were acquired at 7T and range in between the reported values, which is in good agreement with literature, as decreasing T_2 relaxation values are expected with increasing magnetic field strength.

Even though differences between CRT and FID acquisition schemes were found, values were within the standard deviation and on average 5-19% different. This could presumably be caused by differences in the acquisition protocol for FID scans (longer TR , higher number of TI/TE). However, a reliable statistical analysis is difficult given the relatively low sample size of this study ($n_{T_1} = 6$, $n_{T_2} = 3$).

Generally, in vivo T_1 and T_2 relaxation time values of the downstream products Glc and Glx featured high intersubject variability and also regional variability,

i.e., no clear trend was observable and statistically different between GM and WM dominated regions (see table 4.3). This could also be an indication, that there is, potentially no difference between GM and WM in the relaxation time values, but up to this point, no conclusion can be made due to the small sample size and more volunteers have to be measured in the future for a reliable statistical evaluation.

Applying denoising methods, i.e., global low-rank approximation with singular value decomposition or using artificial intelligence, e.g., deep learning methods could potentially improve the sensitivity in the future, which would be beneficial for spectral fitting and potentially reveal regional differences between WM and GM relaxation time constants. Additionally, higher SNR potentially enables relaxation time mapping, increasing spatial resolution or increasing the number of inversion or echo times for future relaxation measurements.

6 Conclusion

In the course of this thesis, a novel 3D MRSI sequence to measure T_1 and T_2 relaxation time constants dynamically with sub-milliliter isotropic resolution was developed.

Using non-Cartesian spatial-spectral sampling of the k -space with density weighting sequence significantly accelerates acquisition times and allows for achieving sufficiently high spatial resolution to reduce partial volume effects substantially to distinguish between GM and WM regions in the brain more reliably. To measure longitudinal and transversal relaxation times Inversion recovery and Hahn spin-echo acquisition schemes were implemented in an interleaved manner, where each trajectory is measured consecutively with variable inversion or echo times. Interleaving relaxation time experiments and measuring the k -space center from inside out minimizes possible effects of fluctuations in Glc and Glx levels by ensuring that data in the center of k -space, which contains high signal amplitude, is acquired at the beginning of the measurement in a short period of time. Additionally, Glc and Glx levels can be monitored during the measurement to check if the concentration levels of the downstream products are stable.

Following successful modification of the sequence tissue-specific relaxation times of deuterium resonances (water, Glc, Glx) were measured in phantom and the human brain in vivo after oral administration of ^2H labeled glucose for the first time.

Only global T_1 and T_2 values are reported in the human brain, thus, tissue-specific (e.g., gray and white matter) relaxation times (T_1/T_2) of deuterium labeled resonances could potentially improve the accuracy of concentration estimation and

the kinetics of energy metabolites (Glc, Glx), representing potential biomarkers of many severe brain pathologies feature regional differences in brain glucose metabolism.

Moreover, the developed sequence is not only limited to a specific nucleus and can be employed to other nuclei i.e. ^1H or ^{31}P MRSI, helping to detect local variations in relaxation times, as often observed for certain pathologies and ultimately improve the accuracy of concentration estimation in future studies.

Bibliography

- [1] E. M. Purcell, H. C. Torrey and R. V. Pound. ‘Resonance Absorption by Nuclear Magnetic Moments in a Solid’. In: *Physical Review* 69.1-2 (1946), pp. 37–38. DOI: 10.1103/PhysRev.69.37.
- [2] F. Bloch, W. W. Hansen and M. Packard. ‘The Nuclear Induction Experiment’. In: *Physical Review* 70.7-8 (1946), pp. 474–485. DOI: 10.1103/PhysRev.70.474.
- [3] W. G. Proctor and F. C. Yu. ‘The Dependence of a Nuclear Magnetic Resonance Frequency upon Chemical Compound’. en. In: *Physical Review* 77.5 (1950), pp. 717–717. DOI: 10.1103/PhysRev.77.717.
- [4] J. T. Arnold, S. S. Dharmatti and M. E. Packard. ‘Chemical Effects on Nuclear Induction Signals from Organic Compounds’. In: *The Journal of Chemical Physics* 19.4 (1951), p. 507. DOI: 10.1063/1.1748264.
- [5] K. L. Behar et al. ‘High-resolution ^1H nuclear magnetic resonance study of cerebral hypoxia in vivo’. eng. In: *Proceedings of the National Academy of Sciences of the United States of America* 80.16 (1983), pp. 4945–4948. DOI: 10.1073/pnas.80.16.4945.
- [6] P. A. Bottomley et al. ‘In vivo solvent-suppressed localized hydrogen nuclear magnetic resonance spectroscopy: a window to metabolism?’ eng. In: *Proceedings of the National Academy of Sciences of the United States of America* 82.7 (1985), pp. 2148–2152. DOI: 10.1073/pnas.82.7.2148.
- [7] Robin A. De Graaf. *In vivo NMR spectroscopy: principles and techniques*. Third edition. Wiley & Sons Ltd, 2019. ISBN: 978-1-119-38254-6.

- [8] P. C. Lauterbur. ‘Image Formation by Induced Local Interactions: Examples Employing Nuclear Magnetic Resonance’. en. In: *Nature* 242.5394 (1973), pp. 190–191. DOI: 10.1038/242190a0.
- [9] P. Mansfield and P. K. Grannell. ‘NMR ‘diffraction’ in solids?’ en. In: *Journal of Physics C: Solid State Physics* 6.22 (1973), p. L422. DOI: 10.1088/0022-3719/6/22/007.
- [10] T R Brown, B M Kincaid and K Ugurbil. ‘NMR chemical shift imaging in three dimensions.’ In: *Proceedings of the National Academy of Sciences* 79.11 (1982), pp. 3523–3526. DOI: 10.1073/pnas.79.11.3523.
- [11] P. Mansfield. ‘Spatial mapping of the chemical shift in NMR’. eng. In: *Magnetic Resonance in Medicine* 1.3 (1984), pp. 370–386. DOI: 10.1002/mrm.1910010308.
- [12] Wolfgang Bogner, Ricardo Otazo and Anke Henning. ‘Accelerated MR spectroscopic imaging—a review of current and emerging techniques’. en. In: *NMR in Biomedicine* 34.5 (2021). DOI: 10.1002/nbm.4314.
- [13] Henk M. De Feyter and Robin A. de Graaf. ‘Deuterium metabolic imaging – Back to the future’. en. In: *Journal of Magnetic Resonance* 326 (2021), p. 106932. DOI: 10.1016/j.jmr.2021.106932.
- [14] Fabian Niess et al. ‘Noninvasive 3-Dimensional ¹H-Magnetic Resonance Spectroscopic Imaging of Human Brain Glucose and Neurotransmitter Metabolism Using Deuterium Labeling at 3T: Feasibility and Interscanner Reproducibility’. eng. In: *Investigative Radiology* (2023). DOI: 10.1097/RLI.0000000000000953.
- [15] Daniel Cocking et al. ‘Deuterium brain imaging at 7T during D₂O dosing’. en. In: *Magnetic Resonance in Medicine* 89.4 (2023), pp. 1514–1521. DOI: 10.1002/mrm.29539.
- [16] Henk M. De Feyter et al. ‘Deuterium metabolic imaging (DMI) for MRI-based 3D mapping of metabolism in vivo’. en. In: *Science Advances* 4.8 (2018), eaat7314. DOI: 10.1126/sciadv.aat7314.

- [17] Loreen Ruhm et al. ‘Deuterium metabolic imaging in the human brain at 9.4 Tesla with high spatial and temporal resolution’. en. In: *NeuroImage* 244 (2021), p. 118639. DOI: 10.1016/j.neuroimage.2021.118639.
- [18] Eulalia Serés Roig et al. ‘Deuterium metabolic imaging of the human brain in vivo at 7 T’. en. In: *Magnetic Resonance in Medicine* 89.1 (2023), pp. 29–39. DOI: 10.1002/mrm.29439.
- [19] William T. Clarke et al. ‘Three-dimensional, 2.5-minute, 7T phosphorus magnetic resonance spectroscopic imaging of the human heart using concentric rings’. en. In: *NMR in Biomedicine* 36.1 (2023), e4813. DOI: 10.1002/nbm.4813.
- [20] Anatole Abragam. *The principles of nuclear magnetism*. eng. International series of monographs on physics 32. Oxford: Oxford Univ. Pr, 1961. ISBN: 978-0-19-852014-6.
- [21] Malcolm H. Levitt. *Spin Dynamics: Basics of Nuclear Magnetic Resonance*. en. Google-Books-ID: bysFAa4MPQcC. John Wiley & Sons, May 2013. ISBN: 978-1-118-68184-8.
- [22] Aizhi Zhu, Daniel Lee and Hyunsuk Shim. ‘Metabolic PET Imaging in Cancer Detection and Therapy Response’. In: *Seminars in oncology* 38.1 (2011), pp. 55–69. DOI: 10.1053/j.seminoncol.2010.11.012.
- [23] Chang-Hoon Choi et al. ‘The state-of-the-art and emerging design approaches of double-tuned RF coils for X-nuclei, brain MR imaging and spectroscopy: A review’. eng. In: *Magnetic Resonance Imaging* 72 (2020), pp. 103–116. DOI: 10.1016/j.mri.2020.07.003.
- [24] Mark E. Ladd et al. ‘Pros and cons of ultra-high-field MRI/MRS for human application’. eng. In: *Progress in Nuclear Magnetic Resonance Spectroscopy* 109 (2018), pp. 1–50. DOI: 10.1016/j.pnmrs.2018.06.001.
- [25] Xiao-Hong Zhu, Ming Lu and Wei Chen. ‘Quantitative imaging of brain energy metabolisms and neuroenergetics using in vivo X-nuclear ²H, ¹⁷O and ³¹P MRS at ultra-high field’. eng. In: *Journal of Magnetic Resonance*

(San Diego, Calif.: 1997) 292 (2018), pp. 155–170. DOI: 10.1016/j.jmr.2018.05.005.

- [26] Ming Lu et al. ‘Quantitative assessment of brain glucose metabolic rates using in vivo deuterium magnetic resonance spectroscopy’. In: *Journal of Cerebral Blood Flow & Metabolism* 37.11 (2017), pp. 3518–3530. DOI: 10.1177/0271678X17706444.
- [27] N. Bloembergen, E. M. Purcell and R. V. Pound. ‘Relaxation Effects in Nuclear Magnetic Resonance Absorption’. en. In: *Physical Review* 73.7 (1948), pp. 679–712. DOI: 10.1103/PhysRev.73.679.
- [28] I. Solomon. ‘Relaxation Processes in a System of Two Spins’. In: *Physical Review* 99.2 (1955), pp. 559–565. DOI: 10.1103/PhysRev.99.559.
- [29] Jozef Kowalewski and Lena Maler. *Nuclear Spin Relaxation in Liquids: Theory, Experiments, and Applications, Second Edition*. English. 2nd edition. Boca Raton London New York: CRC Press, Dec. 2017. ISBN: 978-1-4987-8214-2.
- [30] Robin A. de Graaf et al. ‘High magnetic field water and metabolite proton T1 and T2 relaxation in rat brain in vivo’. eng. In: *Magnetic Resonance in Medicine* 56.2 (2006), pp. 386–394. DOI: 10.1002/mrm.20946.
- [31] Robert D. Johnson et al. ‘Solution deuterium NMR quadrupolar relaxation study of heme mobility in myoglobin’. en. In: *Journal of the American Chemical Society* 111.2 (1989), pp. 481–485. DOI: 10.1021/ja00184a013.
- [32] G. M. Bydder and I. R. Young. ‘MR imaging: clinical use of the inversion recovery sequence’. eng. In: *Journal of Computer Assisted Tomography* 9.4 (1985), pp. 659–675.
- [33] E. L. Hahn. ‘Spin Echoes’. In: *Physical Review* 80.4 (1950), pp. 580–594. DOI: 10.1103/PhysRev.80.580.
- [34] H. Y. Carr and E. M. Purcell. ‘Effects of Diffusion on Free Precession in Nuclear Magnetic Resonance Experiments’. In: *Physical Review* 94.3 (1954), pp. 630–638. DOI: 10.1103/PhysRev.94.630.

- [35] S. Meiboom and D. Gill. ‘Modified Spin-Echo Method for Measuring Nuclear Relaxation Times’. In: *Review of Scientific Instruments* 29.8 (1958), pp. 688–691. DOI: 10.1063/1.1716296.
- [36] A. A Maudsley et al. ‘Spatially resolved high resolution spectroscopy by “four-dimensional” NMR’. In: *Journal of Magnetic Resonance (1969)* 51.1 (1983), pp. 147–152. DOI: 10.1016/0022-2364(83)90113-0.
- [37] Stefan Posse et al. ‘MR spectroscopic imaging: Principles and recent advances’. en. In: *Journal of Magnetic Resonance Imaging* 37.6 (2013), pp. 1301–1325. DOI: 10.1002/jmri.23945.
- [38] Antonin Skoch, Filip Jiru and Jürgen Bunke. ‘Spectroscopic imaging: Basic principles’. In: *European Journal of Radiology. Clinical H MR Spectroscopy* 67.2 (2008), pp. 230–239. DOI: 10.1016/j.ejrad.2008.03.003.
- [39] C. H. Meyer et al. ‘Fast spiral coronary artery imaging’. eng. In: *Magnetic Resonance in Medicine* 28.2 (1992), pp. 202–213. DOI: 10.1002/mrm.1910280204.
- [40] C. B. Ahn, J. H. Kim and Z. H. Cho. ‘High-speed spiral-scan echo planar NMR imaging-I’. eng. In: *IEEE transactions on medical imaging* 5.1 (1986), pp. 2–7. DOI: 10.1109/TMI.1986.4307732.
- [41] E. Adalsteinsson et al. ‘Volumetric spectroscopic imaging with spiral-based k-space trajectories’. eng. In: *Magnetic Resonance in Medicine* 39.6 (1998), pp. 889–898. DOI: 10.1002/mrm.1910390606.
- [42] D. C. Noll. ‘Multishot rosette trajectories for spectrally selective MR imaging’. eng. In: *IEEE transactions on medical imaging* 16.4 (1997), pp. 372–377. DOI: 10.1109/42.611345.
- [43] Claudiu V. Schirda, Costin Tanase and Fernando E. Boada. ‘Rosette spectroscopic imaging: optimal parameters for alias-free, high sensitivity spectroscopic imaging’. eng. In: *Journal of magnetic resonance imaging: JMRI* 29.6 (2009), pp. 1375–1385. DOI: 10.1002/jmri.21760.

- [44] Hochong H. Wu, Jin Hyung Lee and Dwight G. Nishimura. ‘MRI using a concentric rings trajectory’. en. In: *Magnetic Resonance in Medicine* 59.1 (2008), pp. 102–112. DOI: 10.1002/mrm.21300.
- [45] Jon K. Furuyama, Neil E. Wilson and M. Albert Thomas. ‘Spectroscopic imaging using concentrically circular echo-planar trajectories in vivo’. en. In: *Magnetic Resonance in Medicine* 67.6 (2012), pp. 1515–1522. DOI: 10.1002/mrm.23184.
- [46] Wenwen Jiang, Michael Lustig and Peder E. Z. Larson. ‘Concentric rings K-space trajectory for hyperpolarized ^{13}C MR spectroscopic imaging’. en. In: *Magnetic Resonance in Medicine* 75.1 (2016), pp. 19–31. DOI: 10.1002/mrm.25577.
- [47] Adam Steel et al. ‘Metabolite-cycled density-weighted concentric rings k-space trajectory (DW-CRT) enables high-resolution ^1H magnetic resonance spectroscopic imaging at 3-Tesla’. en. In: *Scientific Reports* 8.1 (2018), p. 7792. DOI: 10.1038/s41598-018-26096-y.
- [48] Uzay E. Emir et al. ‘Non-water-suppressed short-echo-time magnetic resonance spectroscopic imaging using a concentric ring k-space trajectory’. eng. In: *NMR in biomedicine* 30.7 (2017), e3714. DOI: 10.1002/nbm.3714.
- [49] Katherine L. Wright et al. ‘Non-Cartesian parallel imaging reconstruction’. en. In: *Journal of Magnetic Resonance Imaging* 40.5 (2014), pp. 1022–1040. DOI: 10.1002/jmri.24521.
- [50] Lukas Hingerl et al. ‘Clinical High-Resolution 3D-MR Spectroscopic Imaging of the Human Brain at 7 T’. eng. In: *Investigative Radiology* 55.4 (2020), pp. 239–248. DOI: 10.1097/RLI.0000000000000626.
- [51] Petr Bednarik et al. ‘ ^1H magnetic resonance spectroscopic imaging of deuterated glucose and of neurotransmitter metabolism at 7 T in the human brain’. en. In: *Nature Biomedical Engineering* 7.8 (2023), pp. 1001–1013. DOI: 10.1038/s41551-023-01035-z.

- [52] Inseok Choi, Hyewon Son and Jea-Hyun Baek. ‘Tricarboxylic Acid (TCA) Cycle Intermediates: Regulators of Immune Responses’. In: *Life* 11.1 (2021), p. 69. DOI: 10.3390/life11010069.
- [53] Husseini Manji et al. ‘Impaired mitochondrial function in psychiatric disorders’. eng. In: *Nature Reviews. Neuroscience* 13.5 (2012), pp. 293–307. DOI: 10.1038/nrn3229.
- [54] Pedro Norat et al. ‘Mitochondrial dysfunction in neurological disorders: Exploring mitochondrial transplantation’. en. In: *npj Regenerative Medicine* 5.1 (2020), pp. 1–9. DOI: 10.1038/s41536-020-00107-x.
- [55] Willem H. Koppenol, Patricia L. Bounds and Chi V. Dang. ‘Otto Warburg’s contributions to current concepts of cancer metabolism’. en. In: *Nature Reviews Cancer* 11.5 (2011), pp. 325–337. DOI: 10.1038/nrc3038.
- [56] Katherine Lameka, Michael D. Farwell and Masanori Ichise. ‘Chapter 11 - Positron Emission Tomography’. In: *Handbook of Clinical Neurology*. Ed. by Joseph C. Masdeu and R. Gilberto González. Vol. 135. Neuroimaging Part I. Elsevier, Jan. 2016, pp. 209–227. DOI: 10.1016/B978-0-444-53485-9.00011-8.
- [57] Dale L. Bailey, ed. *Positron emission tomography: basic sciences*. New York: Springer, 2005. ISBN: 978-1-85233-798-8.
- [58] Stephan Gruber, Vladimir Mlynárik and Ewald Moser. ‘High-resolution 3D proton spectroscopic imaging of the human brain at 3 T: SNR issues and application for anatomy-matched voxel sizes’. en. In: *Magnetic Resonance in Medicine* 49.2 (2003), pp. 299–306. DOI: 10.1002/mrm.10377.
- [59] J. M. B. Kellogg et al. ‘The Magnetic Moments of the Proton and the Deuteron. The Radiofrequency Spectrum of H₂ in Various Magnetic Fields’. In: *Physical Review* 56.8 (1939), pp. 728–743. DOI: 10.1103/PhysRev.56.728.
- [60] I. M. Brereton et al. ‘Preliminary studies on the potential of in vivo deuterium NMR spectroscopy’. eng. In: *Biochemical and Biophysical Research Communications* 137.1 (1986), pp. 579–584. DOI: 10.1016/0006-291x(86)91250-7.

- [61] Fabian Niess et al. ‘Reproducibility of 3D MRSI for imaging human brain glucose metabolism using direct (2H) and indirect (1H) detection of deuterium labeled compounds at 7T and clinical 3T’. In: *NeuroImage* 277 (2023), p. 120250. DOI: 10.1016/j.neuroimage.2023.120250.
- [62] Ewald Moser et al. ‘Windows on the human body–in vivo high-field magnetic resonance research and applications in medicine and psychology’. eng. In: *Sensors (Basel, Switzerland)* 10.6 (2010), pp. 5724–5757. DOI: 10.3390/s100605724.
- [63] Y. Zhang, M. Brady and S. Smith. ‘Segmentation of brain MR images through a hidden Markov random field model and the expectation-maximization algorithm’. eng. In: *IEEE transactions on medical imaging* 20.1 (2001), pp. 45–57. DOI: 10.1109/42.906424.
- [64] S. W. Provencher. ‘Estimation of metabolite concentrations from localized in vivo proton NMR spectra’. eng. In: *Magnetic Resonance in Medicine* 30.6 (1993), pp. 672–679. DOI: 10.1002/mrm.1910300604.
- [65] A. Naressi et al. ‘Java-based graphical user interface for the MRUI quantitation package’. en. In: *Magnetic Resonance Materials in Physics, Biology and Medicine* 12.2 (2001), pp. 141–152. DOI: 10.1007/BF02668096.
- [66] D. Stefan et al. ‘Quantitation of magnetic resonance spectroscopy signals: the jMRUI software package’. en. In: *Measurement Science and Technology* 20.10 (2009), p. 104035. DOI: 10.1088/0957-0233/20/10/104035.
- [67] L. Vanhamme, A. van den Boogaart and S. Van Huffel. ‘Improved method for accurate and efficient quantification of MRS data with use of prior knowledge’. eng. In: *Journal of Magnetic Resonance (San Diego, Calif.: 1997)* 129.1 (1997), pp. 35–43. DOI: 10.1006/jmre.1997.1244.

List of Abbreviations

^1H hydrogen (proton)

^2H deuterium

ADC analog to digital converter

CBF cerebral blood flow

COV coefficient of variation

CRT concentric ring trajectories

FDG fluorodeoxyglucose

FID free induction decay

FT fourier transform

FOV field of view

Glc glucose

Glx glutamate + glutamine

GM gray matter

IDEA integrated development environment for application

Lac lactate

MRI magnetic resonance imaging

MRS magnetic resonance spectroscopy

MRSI magnetic resonance spectroscopic imaging

NMR nuclear magnetic resonance

PET positron emission tomography

POET protocol offline editing tool

PSF point spread function

RF radio frequency

SNR signal to noise ratio

VOI volume of interest

WM white matter

List of Figures

2.1	Magnetization of nuclear spins	7
2.2	Excitation, Relaxation and Induction of nuclear spins	11
2.3	Exemplary ^1H MRS spectrum of the brain	12
2.4	Dipole-dipole interaction	14
2.5	Energy diagram of a dipolar-coupled two-spin state system	16
2.6	T_1 and T_2 dipolar relaxation as a function of the correlation time τ_c	18
2.7	Measuring T_1 relaxation with Inversion recovery	21
2.8	Measuring T_2 relaxation with Hahn spin-echo	22
2.9	Slice Selection	24
2.10	Illustration of a gradient echo MRI sequence	25
2.11	k -space	27
2.12	Schematic illustration of 3D CSI sequence	29
2.13	Schematic illustration of a CRT sequence	31
2.14	Schematic overview of the glucose metabolism in the human brain	33
3.1	Simplified illustration of the original and modified 3D FID ^2H -MRSI sequence	39
3.2	POET and Special Card	41
3.3	7T MR scanner	43
3.4	$^2\text{H}/^1\text{H}$ dual-tuned quadrature bird-cage volume coil	44
3.5	Illustration of the in vivo measurement protocol	46
4.1	Relaxation time maps of the water phantom	51

4.2	Representative exponential fits of relaxation times of the natural abundance water in the water phantom in vitro	52
4.3	Representative exponential fits of relaxation times of the natural abundance water in vivo	54
4.4	Sample spectra in vivo after glucose administration	57
4.5	Representative exponential fits for Inversion recovery experiments in vivo for Glc and Glx	59
4.6	Representative exponential fits for Hahn spin-echo experiments in vivo for Glc and Glx	60

List of Tables

4.1	Relaxation time constants phantom	50
4.2	Relaxation time water in vivo	55
4.3	Relaxation times in vivo for deuterated resonances Glc and Glx	58